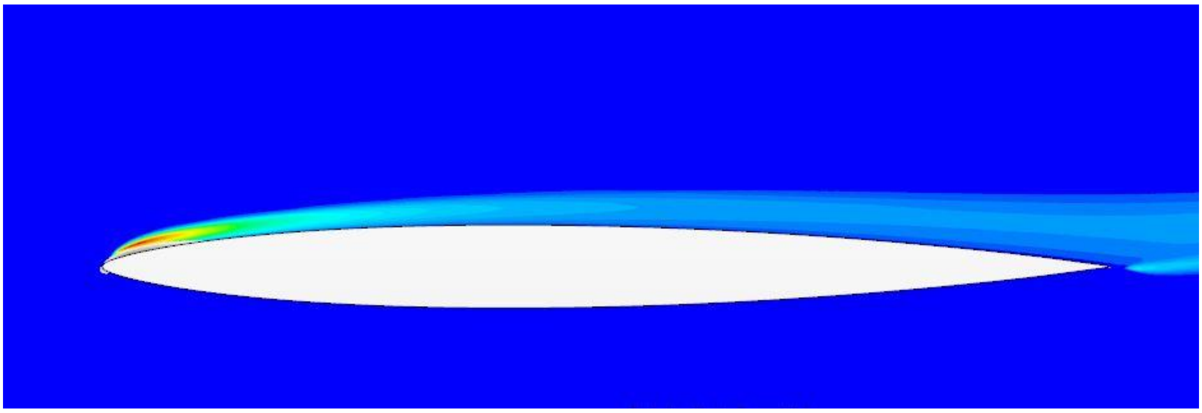

Hydrodynamic analysis of a slalom fin of windsurf board

Ana Marta Rodrigues dos Santos

Thesis to obtain the Master of Science Degree in
Naval Architecture and Marine Engineering

Naval Architecture and Ocean Engineering

Supervisor: Prof. José Manuel da Silva Chaves Ribeiro Pereira
Co-Supervisor: Prof. Yordan Garbatov

Examination Committee

Chairperson: Prof. Carlos Guedes Soares
Member: Prof. Yordan Garbatov
Member: Prof. Sergey Sutulo

December 2018

" "Difficult" and "impossible" are cousins often mistaken for one another, with very little in common."

- Scott Lynch, Red Seas Under Red Skies

"Why do we love the sea? It is because it has some potent power to make us think things we like to think."

- Robert Henri

Acknowledgements

There is a handful of people who made this sailing on stormy seas much easier. Some helped guiding the ship, like: Professor José Chaves Pereira, for his extensive knowledge and clearness in teaching that makes it easy to understand complex problems; Professor Yordan Garbatov, for lighting my interest on the subject and helping this thesis turn into a practical application, which I like; and Dr Leigh Sutherland, that was always kind and interested in helping, tying ends in different disciplines to take the projects to the next level. To Luis Baptista at Vera Navis, with whom discussing these matters was always like exploring. As my employer, he was enduringly understanding of the situation and granted me the space and time to arrive to port. To the people working at LASEF, specially Duarte, for advice and help. To all them, my thanks for the time and guidance.

To my friends at college, Nir and Gorka, for being good mates and for their efforts in the many endeavours. If not for them, these two years would had been boring. It was a pleasure sailing with them.

À minha familia, pela oportunidade de estudar e chegar ao lugar onde estou. Obrigada por todo o apoio e por me levarem sempre em frente, são os melhores pais que podia desejar.

And to my partner and best friend, Francisco, for always believing in me. For the many times we couldn't be together because of college, for the many times he gave me stamina to finish though projects, for always being caring and understanding, this is for you: it's done, let's go!

Abstract

The objective of the thesis is to perform a hydrodynamic analysis in estimating the water-induced loads on a real slalom fin of a windsurf board. First, an initial 2-D flow study of the fin hydrofoil, using the software XFOIL will be performed. This will serve as mean of calibration for the commercial Computational Fluid Dynamics software Star-CCM+. Since the analysed flow is in the range of $3\text{x}10^5$ to $10\text{x}10^5$ of the Reynolds' number, inside the transition interval, laminar, transition and turbulence models will be used. The 2-D flow study of the hydrofoil and the 3-D flow study of the fin will be conducted using Star-CCM+, to analyse the fluid-structure interaction. This MSc thesis will rely on several research collaborations originating from different Universities from Portugal and the United Kingdom, which may lead to an opportunity of a further cavitation phenomenon investigation.

Keywords: CFD, Star-CCM+, Windsurf, Fin, RANS, Hydrofoil, $\gamma - Re_\theta$ transition model, $k - \omega$ SST

Contents

List of Tables

List of Figures

Nomenclature

- U - Velocity
- AoA or α – Angle of Attack
- C_l or C_L – Lift Coefficient
- C_d or C_D – Drag Coefficient
- C_m or C_M – Moment Coefficient
- L – Lift Force
- D – Drag Force
- M - Moment
- p – Pressure
- ρ – Specific Density
- S – Wing area
- c – Chord
- T – Temperature
- Pr – Prandtl number
- q – Heat Flux
- τ – Stress Tensor

Glossary

- CFD – Computational Fluid Dynamics
- SFWB – Slalom Fin of Windsurf Board
- FSI – Fluid Structure Interaction
- LSB – Laminar Separation Bubble
- N-S – Navier-Stokes
- US – Upper Surface
- LS – Lower Surface
- TKE – Turbulent Kinetic Energy

Chapter 1

Introduction

1.1 Motivation

Since the early ages, man has designed and crafted vessels that would help on the task of crossing seas, rivers and oceans. Nowadays, man no longer needs to build for the sole purpose of survival: he can use his crafts for leisure as well. At the marine environment, there are several sports and amusements which require the art and know-how skills of artisans, be it windsurf surfboards or small sailing crafts. With modern technology, it is within reach an in-depth engineering study of these crafted arts. Together in symbiosis, art and engineering may lead to improved performance, taking man faster and further into the future.

This thesis aspires to open a door in the study of crafted windsurf board fins, where an already existing design will be studied and dissected. With the tools available in our century, the flow and fluid-structure interaction can be simulated with accuracy, to pinpoint the aspects of the part that can be improved. Specifically, these tools would be Computational Fluid Dynamics' (CFD), software, a virtual environment where the fin can be pushed to the limits endlessly and at lower costs than those of a towing tank.

1.2 Objectives

This thesis performs a hydrodynamic analysis to a slalom fin for a windsurf board (SFWB). The fin, object of the study, is made by *F-Hot* company, by the designer Steve Cook. The primary objective includes:

- Verify the pressure distribution at the slalom fin of windsurf board.

Aside from the present work, an approach using numerical and experimental analysis to the ultimate strength of the SFWB is being conducted. In the future, the following studies will be performed [2]:

- Fluid-Structure Interaction (FSI) modelling (using data provided with this thesis, to be developed at Instituto Superior Técnico);
- Fin optimisation, using the previously developed models as a design tool;

The creation of a foil for marine sports' applications covers many steps, like the structural engineering, the hydrodynamics, durability, fatigue, etc. Despite the comprehensive checklist, the study will focus on the analysis of the flow around the SFWB. It is intended to understand how the flow will develop inside a velocity envelope, and what will be the hydrodynamic loads on the structure. As such, the fin will first be studied in 2-D, where validation of results can be easily assessed. After, the study will be carried out in 3-D.

1.3 Thesis Structure

Chapter 1 presents the introduction of the studied problem. The second chapter will polish the problem and introduce basic aerodynamic concepts to help understand later the results. The third chapter describes a preliminary analysis to the 2-D aerofoil: this would validate later the results from the CFD software, as well as give a first glimpse of the phenomena taking place.

Chapter 4 describes the selection of the parameters for the CFD analysis and its validation by wind-tunnel data, to be later used on the subjects of Chapter 5 and Chapter 6. The proper 2-D analysis of the fin profile is discussed in Chapter 5, and then Chapter 6 takes it to the third dimension. To finalise, two studies have been added: one of parametric optimisation of the hydrofoil and a second one, that shows the solicitation of the piece by three user types. It has also been included some notes regarding the data obtained in the water tank, that may be found in Chapter 7. Finally, Chapter 8 concludes all the investigation, and Chapter 9 discusses future work.

1.4 Conceptualisation and State-of-the-Art

By the beginning of the 20th century, pure sailing ships gave way to machine-powered vessels and the primary propulsion method for trading and naval ships. However, sailing ships continued to be appraised for recreational uses.

It was for that very purpose that in 1965, S. Newman Darby, an inventor, designed a hand-held sail rig fastened with a universal joint to a floating platform with a tail fin (Figure 1.1). He would name it of sailboarding, as published in *Popular Science Monthly* magazine. He would then manufacture with his brothers these boards in Darby Industries, despite no patent associated.

Figure 1.1: S. Newman Darby steering sailboard backwards on Susquehana River, Pennsylvania (1964)

Figure 1.2: Modern windsurf board

Sailboarding is nowadays known as windsurfing. The name was adopted from Windsurfer International, a company owned by Hoyle Schweitzer and Jim Drake, developed through a patent granted to them on 1970 for a wind-propelled apparatus, that, in essence, was a duplicate of Newman Darby's work of the sailboard.

Darby would win the rights for his invention years later, and continuously improve the windsurf board (Figure 1.2). [3]

Now, windsurfing is commonly known as a surface water sport, joining the sailing and surfing sports. The sailboard will navigate accordingly to the way the sailor manoeuvres the sail, using the boom, and the wind conditions. As expected, the sail must be oriented from the leech to the luff with the wind direction, with the sailor on the lee side. The balance between board, rig and sailor is fundamental to keep sailing/hydroplaning.

The boards are usually 2.5 to 3 metres in length, keeping the rig and the universal joint as a primary feature. The rig now consists of a mast, boom and sail (see Figure 1.3). Depending on the user, conditions and type of windsurfing, the area of the sail may change. Furthermore, to give rigidity to the sail, sometimes battens and batten pockets may be applied, much resembling the Asian junk ship's sails. As for the hull, main features consist on the mast track, where the universal joint fits, the centreboard slit, for the centreboard (a type of retractable fin that is used to oppose the drag force of the sail and sail upwind [4]), the foot straps on deck, to help the raider on manoeuvres, and the piece in analysis on this thesis, the fin, or skeg.

The fin is firmly fitted on the bottom of the board, inside the water. Its primary purpose is to generate lift and assist in the directional control of the board. Typically, the larger the fin, the more lift it will generate, ideally for proportionally bigger sails and lighter winds. Smaller skegs are good for strong winds, for a more manoeuvre sailing style or for taking the first steps on the sport [5]. Thickness is also of importance, as thicker fins generate more power in light wind, but are less efficient when the sailing speed increases. Finally, flexibility is another factor to have in mind when choosing the sailing speed desired: if the fins are stiffer, higher speeds are efficiently achieved, but when manoeuvring, malleable fins win.

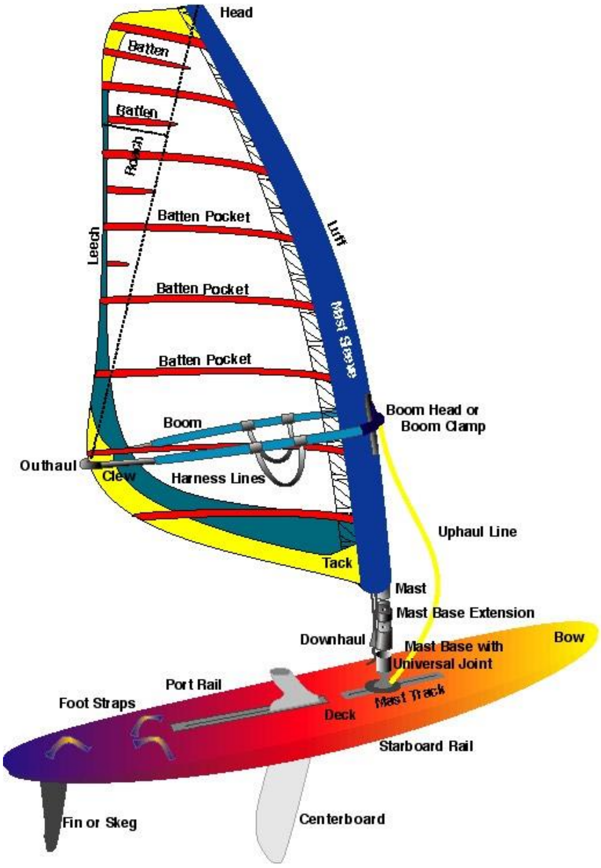

Figure 1.3: Diagram of the different features of a windsurf board.

Of course, soon enough new branches of the sport were sprouting. The fins would also be adapted to the new demands, being distinguished the main types of fins (see Figure 1.4 for some examples):

- Race fins: Very long, straight and slim with maximum stiffness, made in carbon fibre.
- Slalom Fins: Shorter fins, but equally stiff and slim. May be tilted backwards, also made in carbon fibre composites or G10.
- Freeride Fins: About the same length as the fins for slalom, but more flexible and with a curved outline. Primary materials for the composition are carbon composites, G10 or vinyl.
- Freestyle Fins: Wide, short fins, that provide fast planning and good acceleration, also ensuring low resistance during sliding manoeuvres. Materials comprehend G10 or vinyl composites.
- Wave Fins: Short and with a curved outline, are the most manoeuvrable fins, appropriate for wave riding. Can be used in single or multiple fin configurations. Made of G10 or Vinyl composites.

- Bump & Jump Fins: Fins made for sailing on smaller boards but with high winds, also great for leaping, as they provide excellent control and speed, keeping manoeuvrability. Made of G10 or vinyl composites.
- Anti-Weed Fins: These fins possess a highly tilted shape to promote the weed sliding, where the conditions of the water demand. They can have many sizes to fit different sailing styles.
- Shallow Waters' Fins: Half of the length of regular fins, these fins are suited for very shallow waters. As to compensate, the area of the fin increases with its broader and thicker body. Primary materials are G10 or vinyl composites. [6]

Figure 1.3: From left to right: race fin, slalom fin and wave fin (images by EASY/SURF)

Chapter 2

Slalom Fin of Windsurf Board

2.1 Work Description

As windsurfing is becoming more and more a competitive sport (like Formula Windsurf, Slalom competition, or even at the Summer Olympics, for example), there is also the need to amplify the skills of the sailors. Such performance can be achieved with the improvement of characteristics like weight, hull surface friction, sail camber, or, as it will be explored in this thesis, the fin configuration.

Many aspects being materials, the arrangement of composite layers, shape or thickness can be changed; nevertheless, the present aim concerns the nature of the hydrodynamic flow and the estimation of the water-induced loads. The study of an existing slalom fin of windsurf board may lead to a better understanding of its flaws, providing insight into the improvement of new fins.

2.2 Bibliographic Revision

The research of information needed to meet two subjects. First, it had to be a hydrodynamic or aerodynamic study of a profile, and secondly, this study had to be centred on the same flow conditions, specifically Reynolds number. Additionally, some publications are essential and other bibliography is also recommended by the supervisors.

The main publication for aid in CFD analysis in this thesis was *The Finite Volume Method in Computational Fluid Dynamics*, by F. Moukalled [7] while for the basics of aerodynamics is the *Fundamentos de Aerodinâmica Incompressível*, by V. Brederode [8].

A similar dissertation suggested by the supervisors was done by N. Silva on *Parametric Design, Aerodynamic Analysis and Parametric Optimization of a Solar UAV* [9]. This project has many common points in what concerns the nature of the flow and physical models employed at the CFD analysis. Another close project is developed by K. Atkins [10]. Finally, the present dissertation is a continuation of the project developed by F. Nascimento on the numerical and experimental analysis of ultimate strength for the windsurf fin [11].

2.3 Work Case Studies

The hydrodynamic analysis will be conducted using computational fluid dynamics. The case studies for the analysis are:

1. To conduct a pre-analysis in 2-D, for a control aerofoil (E387) and the fin profile. A free software will be used (XFOIL). This will depict a general idea of the range of values, for pressure, lift, drag and other phenomena, to be expected per 3-D analysis;
2. Compare program data obtained for the control aerofoil to wind-tunnel results to verify the legitimacy of the data;
3. After, using Star-CCM+, a 2-D analysis of the control profile E387 will be performed to verify the physics models to employ, comparing to wind-tunnel and XFOIL data.
4. Using Star-CCM+, perform a 2-D flow analysis of the fin profile.
5. To finalise the research, the 3-D analysis of the complete fin will be run on Star-CCM.

2.4 Fin Design and Physical Properties

This chapter aims to establish all the parameters needed to start the analysis. As such, a description of the slalom fin is necessary. After, the mission envelope, consisting on speed, sea parameters (and thus Reynolds number), and angle of attack, will be characterised.

- **37 RS-3 Standard Slalom Fin**

The object in the study is a slalom fin for windsurfing practice, as in Figure 2.1. The total span, excluding the board attachment box, is of 360.17 mm. The length, or chord, at root is 100 mm, the rake angle 2° to the aft.

Figure 2.1: Slalom fin of windsurf board dimensions (all dimensions in mm and degrees)

The leading edge of the piece is to be the round front, and the trailing edge the straight opposite side. The F-Hot company produces the SFWB. Further analysis of the hydrofoil development is carried out in *Chapter 3: Preliminary Analysis*.

- **Trial Envelope**

To perform the study on the SFWB, it is necessary to know the fluid characteristics. The table 2.1 summarises all the needed seawater parameters with a salinity of 35 g/kg [12] [13], sailing parameters [14] and estimations made.

Table 2.1: Trial running parameters

Name	Value	Units
Temperature	20	°C
Density of seawater σ (sea water @ 20 °C)	1024.9	kg/m^3
Kinematic Viscosity υ (sea water @ 20 °C)	1.050×10^{-6}	m^2s^{-1}
Dynamic Viscosity μ (sea water @ 20 °C)	1.077×10^{3}	kg/m.s
Minimum velocity	7.700 (15)	m/s (kn)
Average velocity	10.300 (20)	m/s (kn)
Maximum velocity	25 (50)	m/s (kn)
Minimum Reynolds Number	0.200×10^{6}	
Maximum Reynolds Number	0.750×10^{6}	
Minimum angle of attack	0	°
Maximum angle of attack	15	°

Reynolds number is based on the minimum and maximum length of the SFWB chord, being highly sensitive to this value.

2.5 Aerofoils

Aerofoils are the shape of wings, blades (in propellers, rotors or turbines), or sails (examples on Figure 2.2). In this particular case, it is the cross sectional of the windsurf board fin, also named as a hydrofoil. Typically, aerofoils are associated with gas, air, as a fluid. Nevertheless, the next phenomena can also be found in liquid means – because, if it deforms and flows under shear forces, it is a fluid.

An aerofoil as a specific terminology associated with it. On its geometry, most important are the leading edge (the round border), trailing edge (the sharp border), and chord (see Figure 2.3).

- The leading edge is the point at the front of the aerofoil that as the maximum curvature. The foils are generally oriented with this side to the incoming flow.
- The trailing edge is the point of maximum curvature at the rear of the aerofoil
- Chord, c, is the straight line connecting the leading and trailing edges.
- Camber line is the locus of points midway between the upper and lower surface.

- Thickness, measured perpendicular to the camber line, or sometimes chord line, is measured in chord percentage.

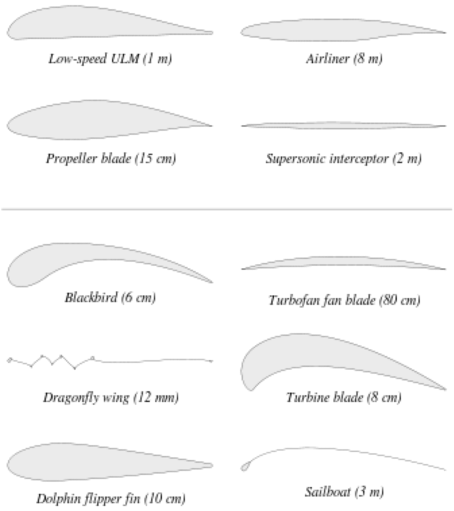

Figure 2.2: Different aerofoils and hydrofoils (Wikipedia images)

If the camber line is not coincident with the chord, then the aerofoil is said to be asymmetric, while if the thickness is equally disposed on the two surfaces, along with the chord, it is symmetric. At the leading, the incoming flow is stagnant, which means the velocity is equal to zero. The angle formed between the chord and relative wind (that has the same vector but opposite direction as the aerofoil motion), is called angle of attack (mind that the chord pointing direction does not necessarily mean it is the object moving direction!).

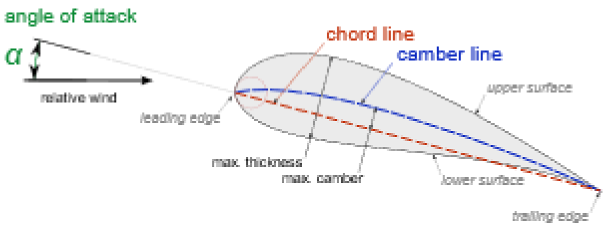

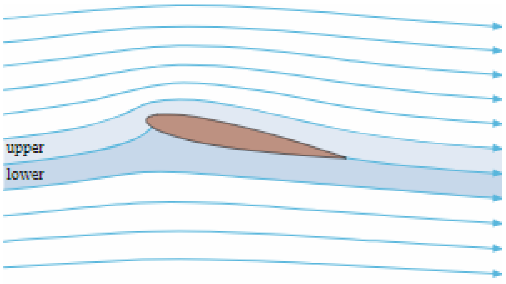

Figure 2.3: Aerofoil/hydrofoil terminology

Figure 2.4: Flow lines around the profile get closer on the upper surface (negative pressure distribution), and apart on the lower surface (positive pressure distribution)

When moving in a fluid with a suitable angle, the aerofoil will generate an aerodynamic force by deflecting the oncoming fluid. This force may be decomposed in two components:

- If the component is perpendicular to the relative wind, it is called lift;
- If it is opposed to the relative wind will be named drag.

What is happening to the flow to generate the aerodynamic force is that, when the relative wind encounters the leading edge, the flow will tend to go around the aerofoil. Typically, on the upper surface, the flow lines will be closer together, since the area available for the flow to pass has reduced. On the lower surface, this area has increased, hence the flow lines will be further apart, as in Figure 2.4. This, by Bernoulli's principle ((2.1), means that if the flow rate is constant, but the areas before and around the aerofoil are changing, then the velocity must change (but only if the fluid is incompressible, with constant density, which sea water is).

$$\frac{v_1^2}{2}+gz_1+\frac{p_1}{\rho}=\frac{v_2^2}{2}+gz_2+\frac{p_2}{\rho} \tag{2.1}$$

Associated with an increase of velocity on the upper surface is a negative pressure distribution; on the lower side, there is a positive pressure distribution, and the velocity diminishes. Thus, there is suction on the upper surface and pressure on the lower surface, all contributing to the generation of the aerodynamic force. On symmetric profiles, an angle of attack of zero degrees does not produce lift, since the flow is equally separated and the distribution of pressures on the two sides nulls each other.

This pressure resultant also has a specific point of application, the centre of pressure (CP), or aerodynamic centre, which is at the chord and is the only point where a moment is not generated. In asymmetric profiles, this point changes with the AoA, but if the profile is symmetric, then the CP position is constant.

To quantify the lift and drag and compare it between aerofoils, these forces can be made non-dimensional, known as C_l and C_d, respectively Lift and Drag coefficients. The coefficients can be easily calculated for 2-D or 3-D profiles as seen in (2.2 and (2.3. As for pressure, to obtain a load that can be used on other works is presented expression 2.4 [8].

$$2D\begin{cases} C_l=\dfrac{L}{\frac{1}{2}\rho V^2 c} \\ C_d=\dfrac{D}{\frac{1}{2}\rho V^2 c} \end{cases} \tag{2.2}$$

$$3D\begin{cases} C_L=\dfrac{L}{\frac{1}{2}\rho V^2 S} \\ C_D=\dfrac{D}{\frac{1}{2}\rho V^2 S} \end{cases} \tag{2.3}$$

$$Cp=\frac{p-p_\infty}{\frac{1}{2}\rho_\infty V_\infty^2} \tag{2.4}$$

2.6 Navier-Stokes and CFD Analysis

When the time comes to analyse the flow development in a CFD program, the computations will be around the Navier-Stokes equations. These equations, presented in non-dimensional reference quantities, consist of a time-dependent continuity equation for conservation of mass ((2.5) and three time-dependent conservation of momentum equations ((2.6 to (2.8) [15]. Solving them for a set of boundary conditions (such as inlets, outlets, and walls), predicts the fluid velocity and its pressure in a given geometry. There are four independent variables along these equations, the x, y, and z are spatial coordinates of some domain, and there is time t. Complementing, are six dependent variables; the pressure p, density ρ, and temperature T (Et is the total energy and contains the temperature), and finally, the three components that form the velocity vector; the u component, correspondent to the x-direction, the v component in y-direction, and the w component, is in z-direction. The six dependent variables are functions of the four independent variables.

$$\frac{\partial \rho}{\partial t}+\frac{\partial(\rho \cdot u)}{\partial x}+\frac{\partial(\rho \cdot v)}{\partial y}+\frac{\partial(\rho \cdot w)}{\partial z}=0, Continuity \tag{2.5}$$

$$\begin{aligned}\frac{\partial(\rho \cdot u)}{\partial t}+\frac{\partial(\rho \cdot u^2)}{\partial x}+\frac{\partial(\rho \cdot u \cdot v)}{\partial y}+\frac{\partial(\rho \cdot u \cdot w)}{\partial z} \\ =-\frac{\partial p}{\partial x}+\frac{1}{Re}\cdot\left\{\frac{\partial \tau_{xx}}{\partial x}+\frac{\partial \tau_{xy}}{\partial y}+\frac{\partial \tau_{xz}}{\partial z}\right\}, X-Momentum\end{aligned} \tag{2.6}$$

$$\begin{aligned}\frac{\partial(\rho \cdot v)}{\partial t}+\frac{\partial(\rho \cdot v^2)}{\partial y}+\frac{\partial(\rho \cdot v \cdot u)}{\partial x}+\frac{\partial(\rho \cdot v \cdot w)}{\partial z} \\ =-\frac{\partial p}{\partial y}+\frac{1}{Re}\cdot\left\{\frac{\partial \tau_{yx}}{\partial x}+\frac{\partial \tau_{yy}}{\partial y}+\frac{\partial \tau_{yz}}{\partial z}\right\}, Y-Momentum\end{aligned} \tag{2.7}$$

$$\begin{aligned}\frac{\partial(\rho \cdot w)}{\partial t}+\frac{\partial(\rho \cdot w^2)}{\partial y}+\frac{\partial(\rho \cdot w \cdot u)}{\partial x}+\frac{\partial(\rho \cdot v \cdot w)}{\partial z} \\ =-\frac{\partial p}{\partial z}+\frac{1}{Re}\cdot\left\{\frac{\partial \tau_{zx}}{\partial x}+\frac{\partial \tau_{zy}}{\partial y}+\frac{\partial \tau_{zz}}{\partial z}\right\}, Z-Momentum\end{aligned} \tag{2.8}$$

On the above equations, there is as expected the Reynolds number, given by Re. This dimensionless number is a ratio of inertial forces to viscous forces, and it used to characterise the type of flow behaviour. Small Re numbers are usually associated with the laminar flow and higher numbers to turbulent flow. Similarly, the Prandtl number, or Pr, is the viscous stresses and thermal stresses ration. After, q and τ are variables of heat flux and components of the stress tensor, respectively.

These equations are too complex to be developed analytically, although some simplifications can be done for simple problems, like *Couette* flow. With computational power is possible to reach some solution for the more complex problems. This problem is dealt with by discretising the domain into finite volumes that do not overlap. The above differential equations can be transformed into algebraic equations and further integrated at each element, in a process also known as Finite Volume Method [7].

- **RANS Equations**

Since the seawater is an incompressible fluid (thus there is no density variation), and of isothermal condition, or by other words, its temperature will not change, the Energy equation usually found on N-S equations will not be used.

Because the flow is incompressible and is expected turbulence in the simulation, the equations above will eventually be changed to the Reynolds Averaged Navier-Stokes (RANS) [7]. These are the typical equations for solving turbulent flow problems; they are based on the decomposition of the flow variables into a time-mean value component plus a fluctuating one, in all governing equations. Equation 2.9 shows how any variable ϕ (like velocity, pressure, temperature), can be decomposed, at a t time and x position, into a mean value $\bar{\phi}$ and fluctuating one ϕ':

$$\phi(x,t) = \bar{\phi}(x,t) + \phi'(x,t) \tag{2.9}$$

When this change is made at the original conservation equations, additional unknowns appear. The act of calculating these new unknown components is called turbulence modelling and will be the object of study further on this thesis.

2.7 Boundary Layer

What is expected of the Navier-Stokes equations to develop is the interaction of the flow with the surface of the aerofoil. The flow around the foils tend to form a boundary layer, as well as around any surface wall, also known as a boundary layer and can develop to two main stages (see Figure 2.5 [1]):

- **Laminar Boundary Layer**

As the flow approaches the surface, the fluid particles immediately next to the wall will adhere to it due to viscous forces, having zero velocity. Upper layers of the flow will progressively gain velocity but keep a laminar shear fashion. As laminar flow extends to the trailing edge, the boundary layer increases thickness. This boundary may be very unstable, and may progress, with due conditions, to the second possible stage:

- **Turbulent Boundary Layer**

This boundary layer has a turbulent flow, with swirls or “eddies”, and is the result of the break in the stability of the boundary layer. It grows quickly as it drags mass from upper layers, having much more energy.

There is also an intermediate stage between the two boundary layers, suitably named transition. This stage does not have fixed frontiers but separates the laminar and turbulent flows around the solid. In some cases, it reattaches, creating the turbulent boundary layer. It sometimes occurs that, whenever the pressure gradient becomes adverse, or by other words when the velocity near the wall changes direction., a laminar separation bubble is created, starting where the laminar flow separates and ending where the turbulent boundary layer begins. The particles closest to the walls will have the opposing direction of the flow, and, as they reach the upper undisturbed layers, the particles are dragged on the flow direction, creating a circular pattern (Figure 2.6 [16]). For Re numbers below 5 x10^5, this bubble will take less than 20% of the chord, making it fit at the short bubble category. For Reynolds number above 5 x10^5, typically this bubble grows, around 20–30% of the chord, and affects the flow drastically. The profile will undergo a drastic drop in the lift, being the cause in aeroplanes for a sudden stall.

For this last boundary to separate, the pressure gradient has to more intensely adverse than the one that caused it, and, if it does separate, the turbulent boundary layer does not reattach.

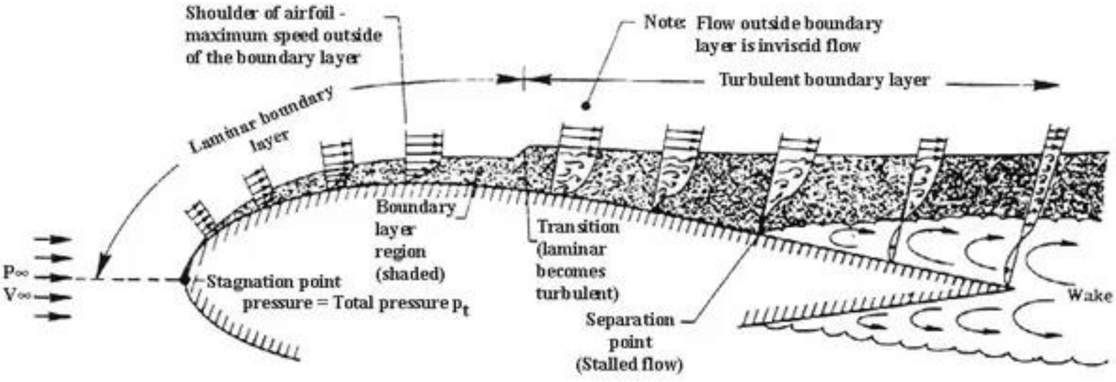

Figure 2.5: Laminar and turbulent boundary layers exemplificative diagram and respective development of the velocity profiles [1]

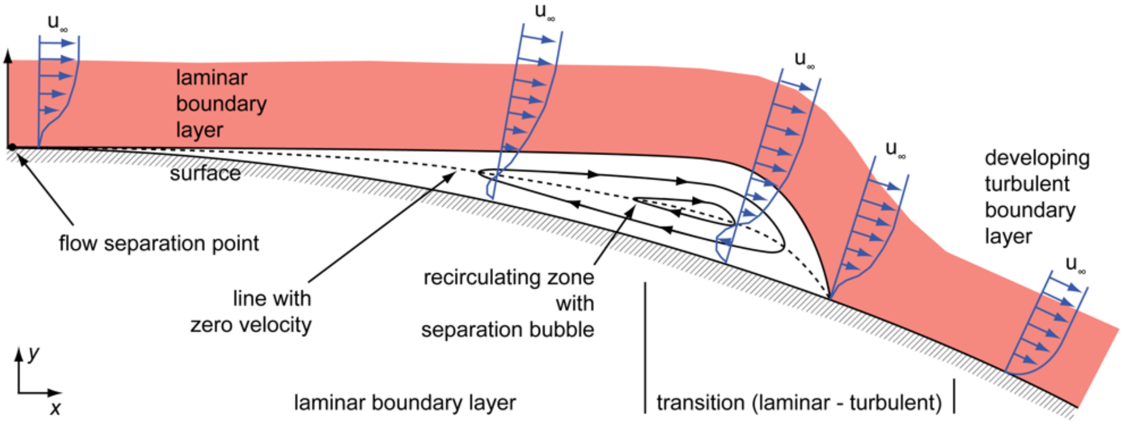

Figure 2.6: Laminar separation bubble [13]

Chapter 3

Preliminary Analysis

3.1 Initial Considerations

Before the 3-D flow analysis, a two-dimensional study of the characteristics of the SFWB was carried out. There are three main reasons why this course of action was taken.

First, it would help understand in which regime (or regimes), the flow was developing. For example, if the flow at the fin is continuously laminar inside the Reynolds interval, then the computation setting may be simplified, as it makes no sense to apply additional models for transition or turbulence, as it will be discussed ahead. Secondly, by running a known profile with results from the wind tunnel, verify that the program is being well used and the results obtained from it can be trusted. Later, the results can be compared to the 3-D flow software and serve as a reference. Moreover, finally, to plot pressure data for other projects, which will not be presented for the sake of shortness.

3.2 Pre-Analysis Software Selection

The two-dimensional flow study was carried out firstly using a non-computational fluid dynamics software. This method is less expensive than wind tunnel experiments and currently produces good results. It is also versatile and generates a significant amount to data in a short time.

This way, this chapter is dedicated to deciding the best software to employ for the 2-D analysis. There are several aspects that the program to be selected had to meet. As the assessment is highlighting a handmade shape, it is essential that this software allow the load of a personalised hydrofoil. Also, it needs to do a viscous study, as it is of high importance to know either or not the flow separates. As this software is to make a preliminary analysis, it does not need to be a high-end program, so an open source or free program will be used.

The main widely used programs available are XFOIL, Javafoil and XFLR5. All these programs are open source.

XFOIL [17] is an interactive program for the design and analysis of subsonic isolated aerofoils. It consists of a collection of menu-driven routines which perform various useful functions such as viscous or inviscid analysis of an existing aerofoil; forced or free transition, transitional separation bubbles, limited trailing edge separation, lift and drag predictions just beyond $C_{L\ max}$, Karman-Tsien compressibility correction, fixed or varying Re and/or Mach numbers. Also allows the writing and reading of aerofoil coordinates and polar save files, plotting of geometry, pressure distribution and multiple polars.

JavaFoil [18] is a relatively simple program, which uses several traditional methods for airfoil analysis. Mainly, it relies on two methods: the potential flow analysis, done with a higher order panel method (linear varying vorticity distribution). Taking a set of airfoil coordinates, it calculates the local, inviscid flow velocity along the surface of the airfoil for any desired angle of attack. The second method, the boundary layer analysis module, steps along the upper and lower surfaces of the airfoil, starting at the stagnation point. It solves a set of differential equations to find the various boundary layer parameters. It is a so-called integral method. The equations and criteria for transition and separation are based on the procedures described by Eppler. As long as the flow stays subsonic, the results are to be reasonably accurate. Usually, this means Mach numbers between zero and 0.5. You cannot analyse aerofoils in supersonic flow with the methods in JavaFoil.

XFLR5 [19] is an analysis tool for aerofoils, wings and planes operating at low Reynolds Numbers. It includes XFOIL's Direct and Inverse analysis capabilities, as well as wing design and analysis capabilities based on the Lifting Line Theory, on the Vortex Lattice Method, and on a 3-D Panel Method.

From all the available software, *XFOIL* is the one that satisfied the above requirements. It combines the fully-coupled viscous/inviscid interaction method with high-order panel methods. For the viscid formulation, the ISES code is used so that the boundary layers and wake are described with two-equation lagged dissipation integral BL formulation and for transition an envelope e^n criterion. The incompressible potential flow interacts with viscous solution via the surface transpiration model, to allow the limited separation regions' calculation. The wake momentum thickness, far downstream, permits the drag calculation. For the inviscid formulation, XFOIL uses the linear vorticity stream function panel method. A source panel models a finite trailing edge base thickness. It is also seen as a reference in data collection in many certified websites and works, is smooth and intuitive to work with. For those reasons, it is the software to be used for the analysis.

3.3 Case Study 1

This validation was done using the SFWB scanned virtual model. The file, in *.igs* format, was treated in *SolidWorks*®. Considering the root of the fin, three profiles where selected, spaced 100 mm in between and starting 100 mm away from the root, like shown (Figure 3.1).

The coordinates that define the three profiles were then extracted. The methodology consisted in applying planes normal to the longitudinal direction, developing from leading to trailing edge. This way, the profile and the plane would intersect, producing a line like an aerofoil. The coordinates in the hydrofoils have an increment of 2 mm along the chord, except at the leading edge, which required refinement, thus, more coordinates.

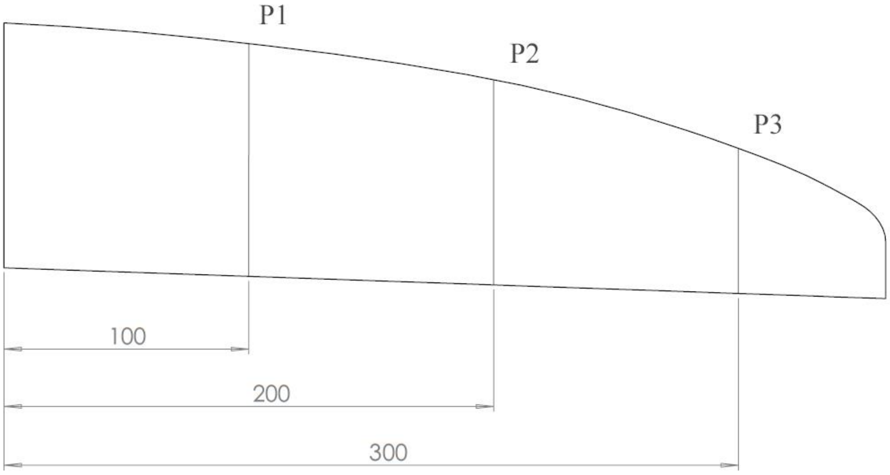

Figure 3.1: location of the three profiles to be studied, named P1, P2 and P3

After, the sets of coordinates would be treated and plotted, like in Figure 3.2 to Figure 3.4. At this point, only half of the profile is plotted, as the hydrofoil is symmetric.

Further investigation revealed that the fin almost has a constant profile in all its extent, aside from the breadth reduction, like explicit on Figure 3.5. This change in maximum thickness and its position is unneglectable.

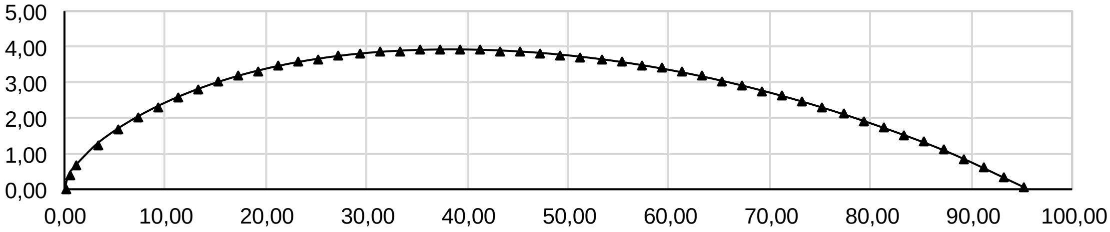

Figure 3.2: hydrofoil P1 at plane 1, 100 mm from root

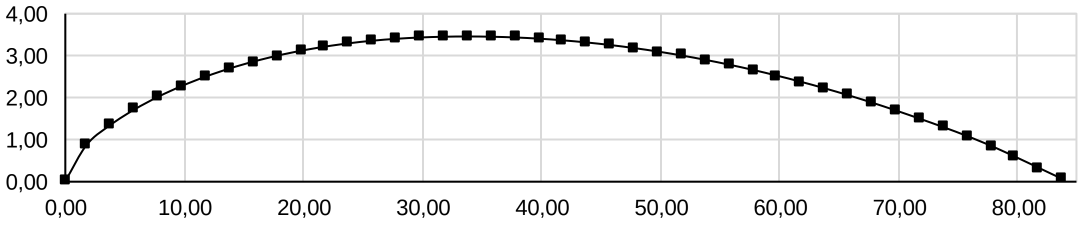

Figure 3.3: hydrofoil P2 at plane 2, 200 mm from root

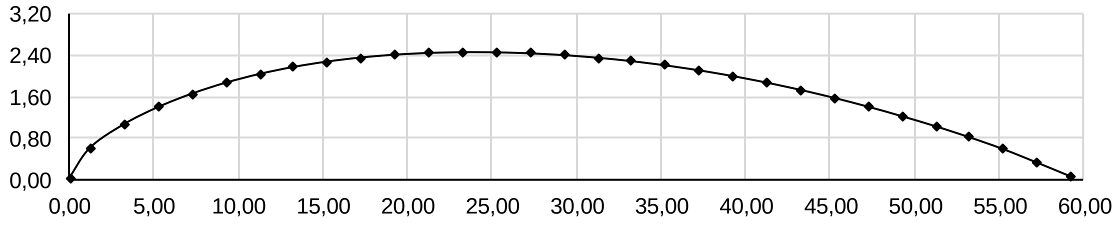

Figure 3.4: hydrofoil P3 at plane 3, 300 mm from root

Table 3.1: thickness and location of maximum thickness along the fin

Name	**Thickness [% of chord]**	**Location [% of chord]**
Plane 1	8.2	41.2
Plane 2	8.2	40.3
Plane 3	8.3	39.2

Then, the hydrofoils were made non-dimensional. This allowed the plotting of the three profiles simultaneously, showing clearly that all three are alike, to the naked eye. For comparison, the fin resembles a NACA 0008, but the later has the maximum thickness location further to the centre of the hydrofoil (Figure 3.5).

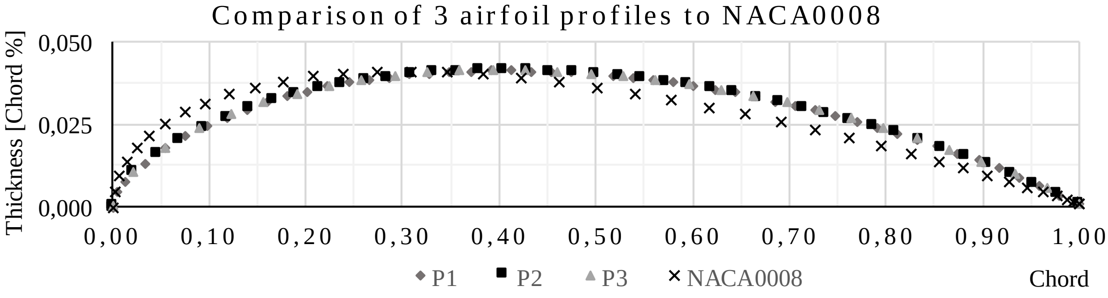

Figure 3.5: Comparison between original hydrofoils and NACA 0008

On further analysis, only the P1 profile will be considered, as the remaining two are the same, but at a different scale. P1 was chosen for the analysis because it is the profile with more coordinates which will produce better results when used on XFOIL. To ensure all conditions are studied, the Reynolds number boundaries were set from the minimum and maximum chord and from the flow velocities.

3.3.1 Initial Stage

With the non-dimensional hydrofoil ready, the coordinates' file was introduced on XFOIL. Some runs were made to feel how the software would work on the coordinates. The tests considered the coordinates in Figure 3.2.

A standard procedure to improve the results, the number of panels of the hydrofoil was set to 160. The viscosity operation was toggled on, and the Reynolds number was set to 0.50 x10^6, with a maximum of 200 iterations to run. In *Analysis* chapter, the typical routine used is explained.

For an angle of attack of 0 degrees, the pressure coefficient distribution is shown below (Figure 3.6).

The red line represents the pressure side and the blue line the suction side. On this chapter C_p distribution Figures, the red and blue lines are overlapping since all Figures represent 0° AoA and symmetric profiles. The dashed line is representing the inviscid pressure distribution.

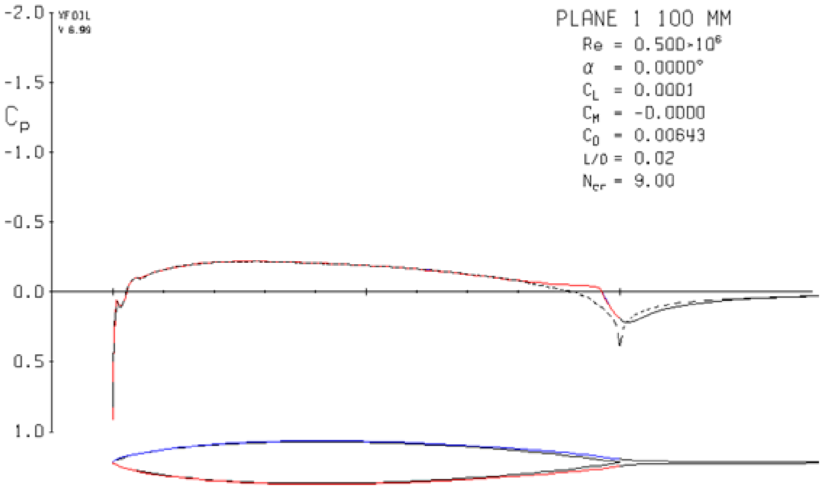

Figure 3.6: Pressure coefficient distribution from p1

It is especially distinguishable an increase in the pressure just after the leading edge on Figure 3.6. Presumably, it is caused by a concavity, present along all the hydrofoil, that induces a contrary pressure gradient.

This feature is incorrect and is a possible result from the SFWB scanning process.

To mitigate the pressure coefficient irregularity, several fairing techniques where sought. First, several splines where adapted to the curvature. This adaptation was carried out using spreadsheet functionalities and formulas, but the results were not satisfactory. The second attempt consisted in reshaping manually the coordinates, as for adding coordinates or simply shifting them.

This aimed at a smoother transition between panels, later, on XFOIL, as the angle between panels was smaller. The adaptation for the first profile is shown in Figure 3.7.

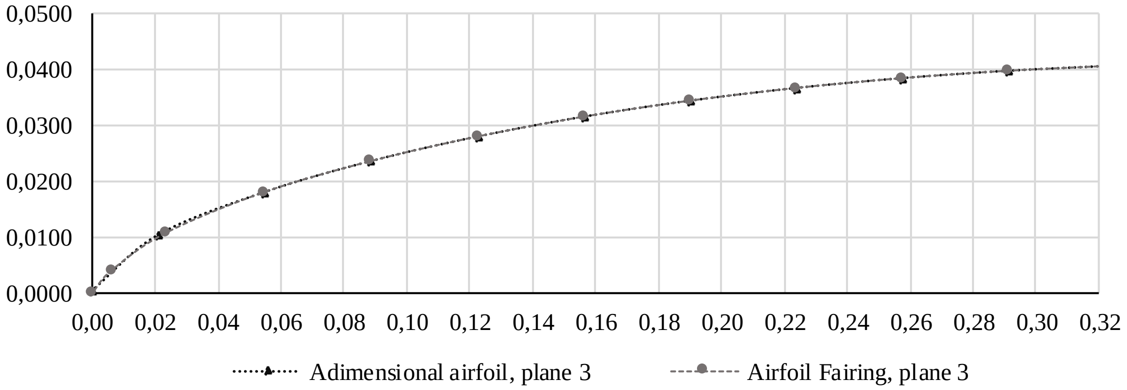

Figure 3.7: Comparison between original coordinates from SFWB and the faired hydrofoil

Each new change was then experimented on XFOIL until the pressure distribution was to resemble a normal hydrofoil. The most important iterations are stored in *.txt* files, with the following name code:

File name:	*pxyy.txt*
[p]:	*plane*
[x]:	*profile number*
[yy]:	*iteration number*

Next is presented the pressure coefficient distribution of the last iteration (number 13), from profile *P1*, with coordinates found on Appendix A.1, and the *NACA 0008* (Figure 3.8 and Figure 3.9). Both computations are at Re 0.46 x10^6 and with AoA of 0°.

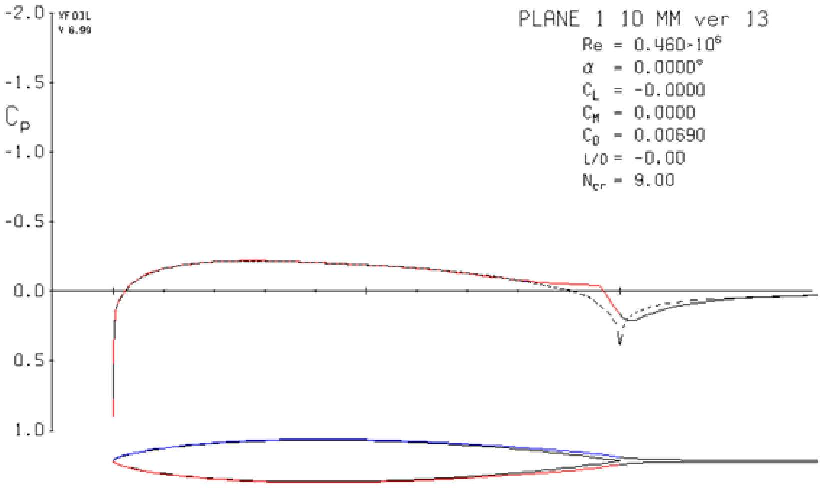

Figure 3.8: Pressure coefficient distribution from profile P113 at Re 0.46 x10^{6}and AoA 0°

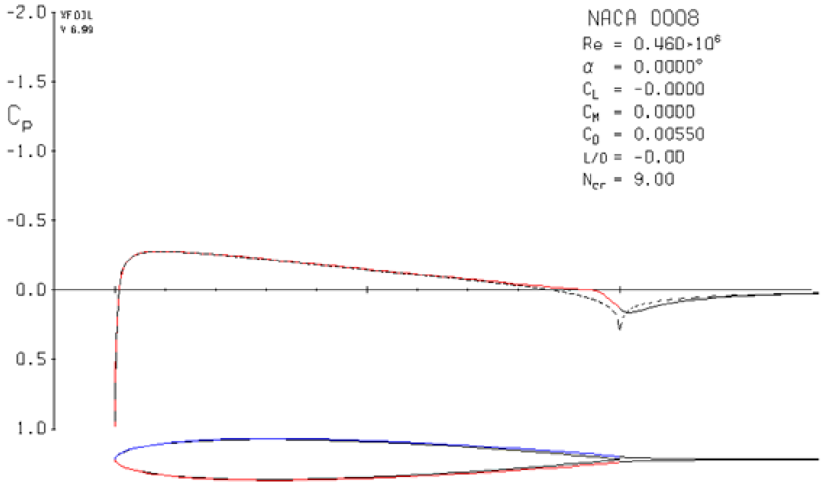

Figure 3.9: Pressure coefficient distribution from profile NACA 0008 at Re 0.46 x10^6 and AoA 0°

When more results were to be extracted, for higher AoA's, it was hard to obtain a solution, as the program could not converge. This may mean some flow anomaly is present and will be investigated after.

This was still no guarantee that the software was being well used and presenting valid results. As such, a known profile, with wind tunnel processed data, was chosen. The idea was to recreate the same conditions as the test but on XFOIL and compare the results.

If the validation proves successful, the faired geometry will be used to retrieve the flow data from the software.

3.4 Analysis

XFOIL software shows a DOS environment, thus, all commands must be typed, and special rules must be followed. A typical routine on XFOIL is explained below.

```
XFOIL c> load pxxx.txt
```

Loads the coordinates file

```
XFOIL c> pane
```

Increases the panel number up to 160

```
XFOIL c> OPER
```

Enters the Operation menu

```
OPERi c> ITER 500
```

Defines number of iterations

```
OPERi c> VISC [RE]
```

Toggles on the viscous effects at Reynolds number [RE]

```
OPERi c> p
```

Toggles on the polar accumulation

```
OPERi c> pxxx_[RE]_polar.txt
```

File name for polar saving

```
OPERi c> Enter
```

Disable dump file

```
OPERi c> SEQP
```

Plot polar during point sequence (optional)

```
OPERi c> A i
```

Specify alpha

```
OPERi c> CPWR pxxx_[RE]_CP0i.txt
```

Write Cp (x) distribution to a text file

...

```
OPERi c> A 16
OPERi c> CPWR pxxx_[RE]_CP16.txt
OPERi c> QUIT
```

Exits the program

The simulations were done between Reynolds 0.20 x10^6 and 0.70 x10^6, with increments of 0.05 x10^6. Since the tests will be done at such low Reynolds number, it is expected the presence of a laminar separation bubble, like it is typical at such values.

Due to the nature of the hydrofoils, very rarely the routine was followed like above until the end. Typically, the program could not converge at some point, usually around the AoA of 5 degrees. One bypass for the problem was to increase the angle by one decimal. A smaller gap between computations seemed to help. Another technique was to jump to 10 or 9 degrees and slowly approach smaller angles. This may mean some anomaly is happening at some angle interval.

3.5 Case Study 2

As validation for the obtained results from XFOIL, a known profile with wind tunnel data was processed on the program. The objective is to compare the results, from the experimental method and the computational method.

- **E387 Wind Tunnel Data**

The chosen profile is an Eppler 387 foil (3.10), with a maximum thickness of 9.1 % at 31 % of the chord. This profile has a 3.2 % camber at 44.8 %, not symmetrical like the SFWB profile being evaluated. Still, has a close thickness and the data found is inside the Reynolds number envelope.

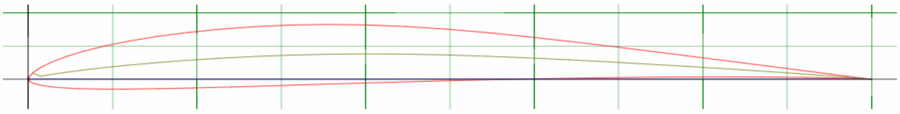

Figure 3.10: Eppler 387 foil (in pink)

The data taken on the E387 originates from the results from NASA Langley taken in the Low-Turbulence Pressure Tunnel (NASA LTPT) [20]. The tests collected data from several Reynolds numbers; the Re of 0.46 x10^6 was seen as appropriate for the study. Then, the fluid velocity condition was recreated on XFOIL, and the results drawn are present in Figure 3.11.

For the lift and drag coefficients, it is safe to conclude that the two tests behave very similarly up until 10 degrees. Above that, it is expected that the fluid boundary layers separate, entering a realm of analysis in which the XFOIL program is not so precise.

As for the momentum coefficient, the results are only close up to 5 degrees. These results are different because the pivot point where the profile is allowed to rotate is different. As standard, XFOIL uses 1/4 of the chord.

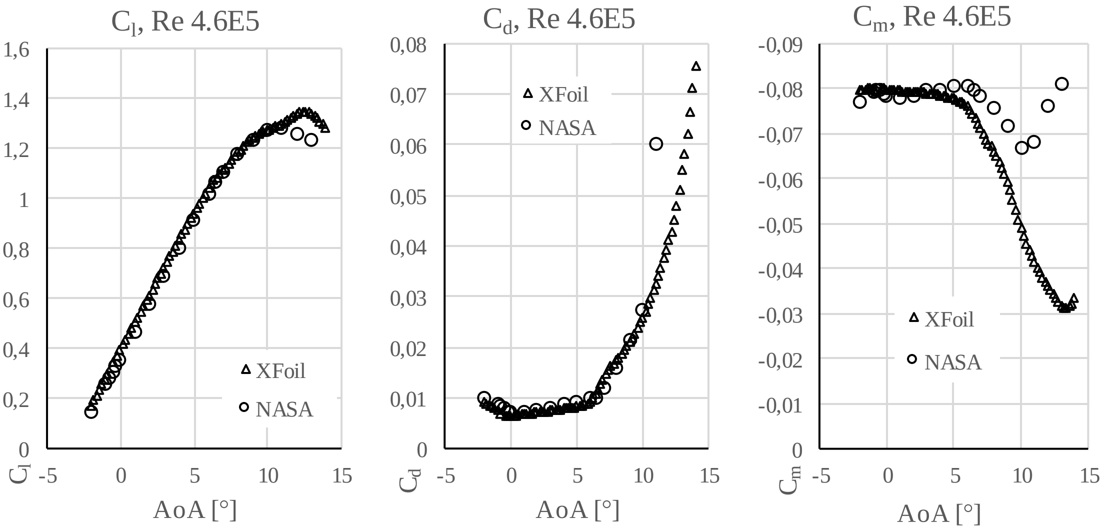

Figure 3.11: Plots for the C_l, C_d and C_m coefficients on E387, using Nasa wind tunnel results and XFOIL results

3.6 Results Discussion

Considering the determined consistency of the results from the last chapter, it is assumed that the program is being properly used. Likewise, this chapter considers the results taken from the profile P113, obtained with XFOIL.

These results comprehend the data observed on XFOIL software, for the Reynolds numbers between 0.20 x10^6 to 0.70 x10^6. The angle of attack ranges from 0° to 16° (in some cases to 15° due to difficulties in convergence).

The pressure coefficient distribution (example in Figure 3.8), plotted to represent the non-dimensional pressure on the surface, shows as expected, a maximum value at the nose of the profile at zero degrees. If the flow was inviscid, that value would also be of one at trailing edge. As the angle increases, different values of pressure coefficient are plotted for the upper surface and lower foil surface. As commonly known, at positive AoA and symmetric aerofoils, the pressure is negative on the upper surface and positive on the lower surface. This effect is broadly used to achieve lift on aeroplanes, as the wings are oriented initially on positive AoA's. To make the reading of the plots more intuitive, the scale has been reversed, being presented the negative values "above zero". Still, regarding this distribution, it was noticeable a smoother slope very close to the tip of the hydrofoil, on the upper side. This shows that the original C_p was to follow a certain degree of degradation, but something unexpected provoked a more severe increase in pressure, which hints for a recirculation bubble.

The lift coefficient presents, as expected for a symmetric foil, a value of zero at AoA 0°. It shows a linear behaviour generally until 6°; after that, it enters the stall (loses sustentation). Around 9°, the aerofoil seems to regain lift, increasing exponentially. For the first part, on the linear behaviour, the Cl reaches around 0.65; on the second half of the lift coefficient distribution, the value may go until 0.72. These coefficients may be converted into forces later.

Regarding the drag coefficient curve, it is starting close to zero at AoA 0°. This is where the drag is minimum, as the profile is in line with the flow. It is seen to increase as the angle of attack increases, parallel to the growth of the exposed area, in the way of the flow lines. The minimum observed value is of 0.0049, and the maximum of 0.203.

The moment coefficient, or pitching moment, is zero when no pitch is observed, congruent with the expected behaviour. From 0° to 5°, the moment is negative, thus applying a momentum that makes the nose of the foil point to the ground. From 5° to 10°, the moment is positive, forcing the leading edge up. After, the momentum turns negative once more. This fits the behaviour watched on the lift coefficient: as the momentum is created by the aerodynamic force shifting (like mentioned before, composed by lift and drag force components).

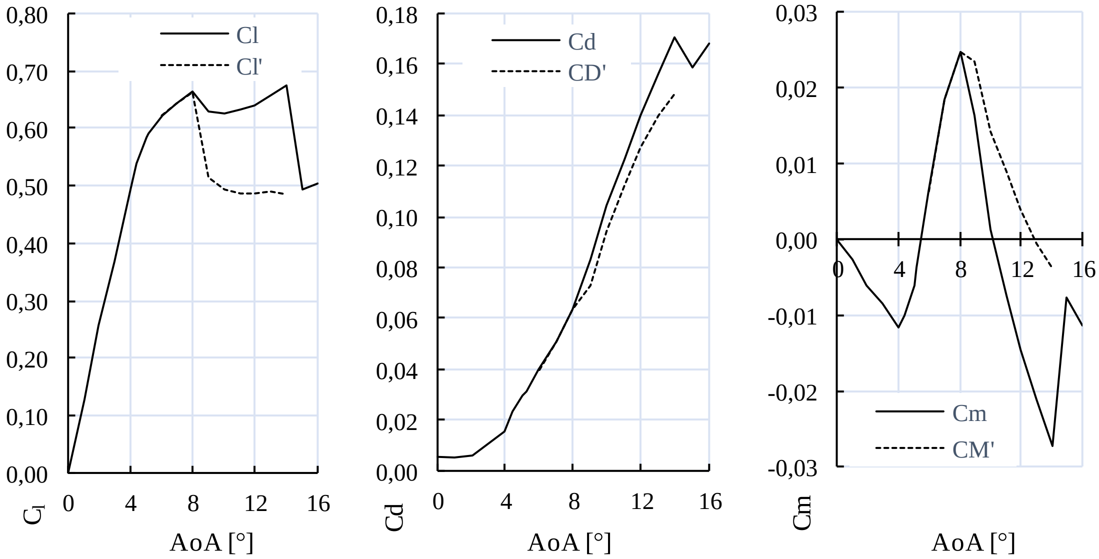

Figure 3.12: Plots for the C_l, C_d and C_m coefficients and transition coordinates on P113, XFOIL results

Tests refer to the trial at Re 6.0x10^5. The duality of results is achieved by solving first from small to large AoA's, and after from higher to smaller AoA's.

The analysis of the transition points of the flow, on both sides of the foil, reveals that on the lower surface, the flow adheres practically until the trailing edge, to the AoA full interval. On the upper surface, the flow stays laminar until 97 % of the chord at 0°, then around 2°, the separation point shifts abruptly to the leading edge, around 4 % of the chord. This value decreases until it can be accepted it separates on the leading edge itself.

Aside from these results, it is important to point out that some trials were made starting at angles such as 14°, progressing to lower angles. New and different values for the coefficients were observed, adding the previously obtained results. This is seen in Figure 3.12, where C_l, C_d and C_m are plotted.

This leads to the conclusion that the software is finding multiple solutions for the same problem. As such, it is safe to assume that some anomaly is occurring, which may also help explain why the transition point changes abruptly after a given angle. Plus, would explain the difficulty in achieving convergence on the results, as multiple solutions seem to be possible.

In sum, transition on the upper surface of the foil is to be expected, like recurrent for the low Re. Some recirculation phenomena seem to be occurring and shall be explored sequentially in the next chapter, where a more powerful CFD tool is to be used.

Chapter 4

Mesh, Turbulence and Transition Model

The following case study comprehends the use of the control aerofoil to verify which are the most appropriate conditions to run the fin profile. In that matter, the choice of software, as well as the mesh and physics models, are important to capture accurately and realistically the flow around the profile. The Reynolds number is the same as previously used on case study 1.

4.1 CFD Software Selection

Similarly, to what was done before, the software to be used was chosen from an array of possible choices. The main characteristics needed concern aspects such as the physical models, the simplicity and ease of use, and the ability to obtain the desired results (lift, drag, pressure coefficients, etc.).

There are some programs available on the market: some are open source and free, but lack interface; others require an active license and server constant connection and others yet, can group many modalities, like mesh generation, flow or multiphysics simulations and so on.

Ansys Fluent [21] program has the capacity to develop many physical models, from laminar to turbulent, but lacks some of the new, cutting-edge transition models. It does offer interesting wall treatments. The advantage is that it conciliates structural mechanics and fluid mechanics disciplines, which can be used later to perform the fluid-structure interaction.

Star-CCM+ [22] also performs such analysis. This software is best known for its ease in use, as well as a vast portfolio of models and parameters that may be tuned, in the fluid analysis. It also has a robust meshing system, can read macro files and create geometries. It is vastly used at master thesis with a CFD approach.

Finally, OpenFOAM [23] is probably the most well-known of the listed, but also the most complex to operate. It is a fully open source software with constant updates, performs meshing, can solve complex flow analysis, such as turbulence, heat transfer, chemical reactions or even electromagnetics. Due to being free software, it has a large user base. That is a positive aspect of having in mind if operating with OpenFOAM, as no GUI interface is available yet and much experience is needed to obtain results.

The used software will be Star-CCM+, due to its availability and support at the Laboratory of Fluid Simulation in Energy and Fluids (LASEF), at the Instituto Superior Técnico (IST).

4.2 Star-CCM+ Aerodynamic Models

The first step in solving the problem would have to be the physics' model selection. Different models need different mesh parameters, as explained below. From the low Reynolds numbers used on this investigation, it is safe to assume that the laminar boundary layer is very unstable and will separate at some point along the wall. As separation occurs, the flow will have a transient state and a turbulent state further downstream. If the turbulent flow reattaches, there will be a separation bubble between the separation zone and reattachment. The Re and the shape of the foil influence the length of this bubble, which can be classified of short or long, the last known to be formed at Reynolds number above 5 x 10^5 [24]. This means that the separation bubble will have, eventually, different lengths along the fin.

Thus, the models should contemplate transition. A brief explanation of the turbulence models employed follows:

4.2.1 SST *k – ω* Turbulence Model

The $k - \omega$ SST turbulence model, developed by Menter, is a combination of two well-known models: the $k - \varepsilon$ and the $k - \omega$. The $k - \varepsilon$, developed by Jones and Launder is a good predictor in fully turbulent flows where the effects of molecular viscosity are neglectable. It is usually used best on high Re numbers. On the other side, the $k - \omega$, by Wilcox, performs best at wall integration and is a good predictor for flow separation [25]. This way, by changing the ε to $k\omega$ on the $k - \varepsilon$ equation, the two models blend near-wall effects, and outer layer effects are captured, resulting in a versatile model:

$$\frac{\partial}{\partial t}(\rho k) + \frac{\partial}{\partial x_i}(\rho k u_i) = \frac{\partial}{\partial x_j}\left(\Gamma_k \frac{\partial k}{\partial x_j}\right) + G_k - Y_k + S_k \tag{4.10}$$

$$\frac{\partial}{\partial t}(\rho \omega) + \frac{\partial}{\partial x_j}(\rho \omega u_j) = \frac{\partial}{\partial x_j}\left(\Gamma_\omega \frac{\partial \omega}{\partial x_j}\right) + G_\omega - Y_\omega + D_\omega + S_\omega \tag{4.11}$$

On the above, the diffusivity is present in Γ_ω and Γ_k. The turbulent kinetic energy generation and specific dissipation rate are given by the variables G_ω and G_k. The Y_ω and Y_k are representing the dissipation and the S_k and S_ω the source terms. Finally, to blend the two models, the variable D_ω is the extra cross diffusion with the formula:

$$D_\omega = 2(1 - F_1) + \rho\sigma_{\omega},2\frac{1}{\omega}\frac{\partial k}{\partial x_j}\frac{\partial \omega}{\partial x_j} \tag{4.12}$$

4.2.2 $\gamma - Re_\theta$ Transition Model

Once it is to be determined if the flow is fully turbulent or if the transition occurs somewhere along the surface, the present model is also in scope. The $\gamma - Re_\theta$ was developed specially for transition flows and combines the SST K-ω with intermittency γ and a transition triggered by a specific local Re. In this case, Re_θ symbolises the critical Re number at which the intermittency will start [26].

This phenomenon is given by [27]

$$\frac{\partial(\rho\gamma)}{\partial t} + \frac{\partial \rho U_j \gamma}{\partial x_j} = P_x\gamma 1 - E_{\gamma 1} + P_x\gamma 2 - E_{\gamma 2} + \frac{\partial}{\partial x_j}\left[\left(\mu + \frac{\mu_t}{\sigma_\gamma}\right)\frac{\partial \gamma}{\partial x_j}\right] \tag{4.13}$$

$$\frac{\partial(\rho R\bar{e}_{\theta t})}{\partial t} + \frac{\partial(\rho U_j R\bar{e}_{\theta t})}{\partial x_j} = P_{\theta t} + \frac{\partial}{\partial x_j}\left[\sigma_{\theta t}(\mu + \mu_t)\frac{\partial R\bar{e}_{\theta t}}{\partial x_j}\right] \tag{4.14}$$

As for coupling the transition on the SST K-ω, the K- equation is modified as:

$$\frac{\partial}{\partial t}(\rho k) + \frac{\partial}{\partial x_i}(\rho k u_i) = \frac{\partial}{\partial x_j}\left(\Gamma_k \frac{\partial k}{\partial x_j}\right) + G_k^* - Y_k^* + S_k, G_k^* = \gamma_{eff}\bar{G}_k \; and$$
$$Y_k^* = \min(\max(\gamma_{eff} 0.1), 1.0)Y_k \tag{4.15}$$

However, attention must be given to wall Y^+ modelling: if the mesh does not allow $Y^+ \leq 1$, the viscous sublayer effect will not be captured and the transition models are working above will not be properly modelled.

4.3 Mesh Characteristics

For the models to work accordingly to the desired, the mesh definition was an iterative process. If the grid created was too coarse, the boundary layer phenomenon would not be captured, but a mesh too much refined takes a long time to be computed.

In total, polyhedral elements and prism layers are the building blocks, with the added feature of surface remesher, available on Star-CCM+. For the boundary between hydrofoil and domain, the prism layer was used, as traditional. This is a layer that tends to follow the surface of the boundary, and, for modelling the boundary layer, proves efficient.

In an attempt to obtain shorter times for the mesh creation, the domain was divided into areas, which would allow a tune of the mesh characteristics inside each. This way, besides the main three-dimensional domain there are smaller volumes: V1.0, V2.0 and V3.0. The volume V1.0 contains the hydrofoil and the two other volumes. The volume V2.0 contains again the aerofoil and V3.0, but much closer to the walls. Its purpose is to refine only the cells at the surface. Finally, V3.0 is composed by V3.1, refining the leading edge and V3.2 the trailing edge. The chord length defined is 100 mm, which is equivalent to the length at the root of the SFWB. The three volumes and domain dimensions are in table 4.1. The thickness is, as common practice, 5% of the chord length.

Table 4.1: domain and control volumes' dimensions

Name	Width [chord lengths]	Height [chord lengths]
Domain	20	15
V1.0	3	1
V2.0	1.2	0.2
V3.1	0.013	0.04
V3.2	0.025	0.01

These volumes were used on case study 3 and 4, except for V3.2 on case 3, which did not need refinement. Associated to them are the element sizes. The idea was to have significant elements near the inlets and outlet and a very fine mesh around the profile and after the exit slab. So, the main domain has elements that can be five times bigger than the hydrofoil chord, with a rate ruling the cell contraction until the boundaries of the control volumes. Table 4.2 sums the input parameters for the mesh creation and Figure 4.1 depicts the final result. Except the values stated, all the remaining values were left as standard. All the values are in absolute dimension.

Table 4.2: domain and control volumes' mesh parameters

Name		Mesh Continuum	
Base Size [m]		0.5	
Nº of Prism Layers		30	
Prism Layer Stretching		1.15	
Prism Layer Thickness [m]		0.005	
Surface Growth Rate		1.08	
Surface Absolute Minimum Size [m]		2.0E-4	
Surface Target Size [m]		1.0	
Control Volumes:	**V1.0**	**V2.0**	**V3.0**
Polyhedral base size [m]	0.001	2.8E-4	3.2E-5
Nº of Prism Layers	-	30	-
Prism Layer Stretching	-	1.15	-
Prism Layer Thickness [m]	-	0.0035	-

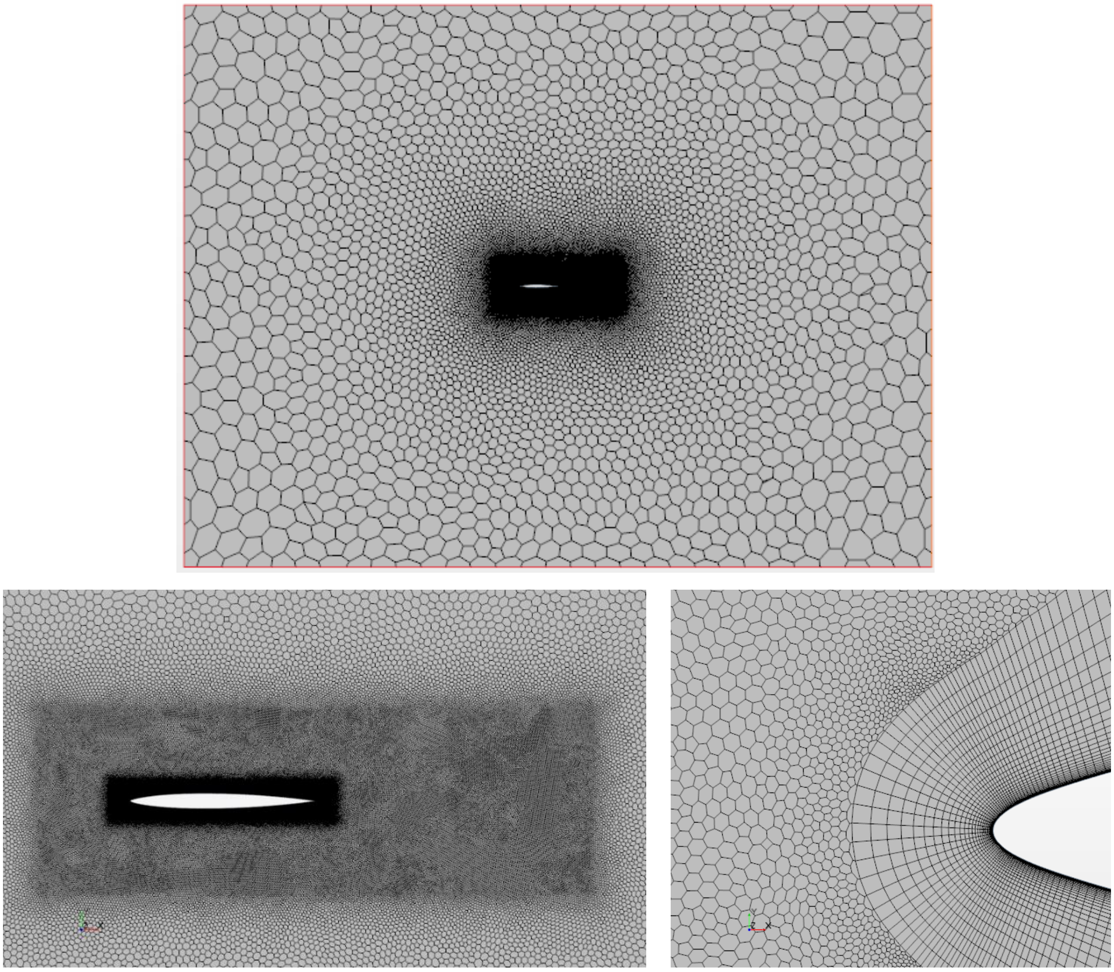

Figure 4. 1: Mesh definition

One of the main challenges was to develop a mesh that would lay around both aerofoils smoothly. The leading edge on the SFWB was the trickiest zone: because the fin is very slim, the curvature would be truncated in faces, decreasing the detail degree. Also, a very thick prism layer, with constant aspect ratio produced large cells at the tip, which is not favourable for the analysis. So, the solution was to divide the control volumes like explained above, with a smaller prism layer thickness and small cell dimension, assuring a good fit around the geometry on both cases.

4.4 Case Study 3

Much like case study 1, the present case aims to verify the most realistic conditions to perform the analysis. As stated, the E387 profile will be studied, operating the mesh and models described previously. The results to be shown are the result of several iterations and the most interesting to be presented.

The conditions of the precedent tests were simulated. As the hydrofoil is now a finite and defined solid, the inlet condition, the Reynolds number, had to be accordingly translated into velocity.

So, the velocity to be used in the test is given by:

$$Re = \frac{Uc}{\upsilon} \Leftrightarrow U = \frac{\upsilon \cdot Re}{c} \Leftrightarrow U = \frac{1.05E-06 \cdot 4.6E5}{0.1} \Leftrightarrow 4.83\ m \cdot s^{-1} \tag{4.16}$$

The different angles of attack will be obtained by rotating the virtual laboratory referential, so all the conditions are maintained through the analysis. The fluid to be simulated is water, with dynamic viscosity from table 2.1.

The simulation setup consisted of applying the next models: two-dimensional, segregated flow, liquid (at constant density), turbulent, $k-\omega$ SST turbulence model and low Y^+ wall treatment. Two simulations for each angle are performed: with transition model $\gamma - Re_\theta$, and without transition model. The objective is to determine which provides the closest results to the experimental data.

At the inlet, the turbulence intensity and turbulent length scale were, as good practice demands, of 0.1% and 10% of the hydrofoil thickness, respectively.

When simulating solely with the $k-\omega$ SST turbulence model, typically the residuals converge efficiently. That is why it is much used when the flow is known to be turbulent from the start. In some cases, the residuals would stall at a value above 10^5 because $k-\omega$ SST failed to find the transition point on the surface, an understandable feature for a turbulence model. To bypass this problem, two ways where used: the first one consists in changing the inlet velocity for one or two iterations length. This would disturb the flow and help the model find the transition point. Another way and the one that proved most effective was changing the relaxation factor. The values applied are between 0.3 and 0.7, always lower than the predefined.

For the $\gamma - Re_\theta$ model, the residuals did not converge using a steady state solver. To obtain valid values, the implicitly unsteady solver would be toggled on. Then, by changing the time step time and the number of inner iterations, the residuals where made drop by 2 orders. The solution found is stationary (oscillations of force coefficients of 10^{-5} decimal). Again, when needed, the relaxation factor is changed between the previous interval. The wall Y^+ was kept under 1 in most of the foil surface.

Using the data compiled, the results from both models were then compared to the wind-tunnel and XFOIL points. On Figure 4.2 are presented the lift and drag coefficients from the four different sources. For the lift coefficient, both models provide satisfactory results. The $k-\omega$ SST model shows a slightly higher value for the peak of the curve, with a maximum error of 6 %. The $\gamma - Re_\theta$ models this quantity with more accuracy and more times, meaning the deviation from the wind-tunnel data is more often with errors below 2 %. That is also true for the drag coefficient, until around 8 degrees where the error is below 9 %. The $k-\omega$ SST model has an overall less good performance, with errors reaching 52%.

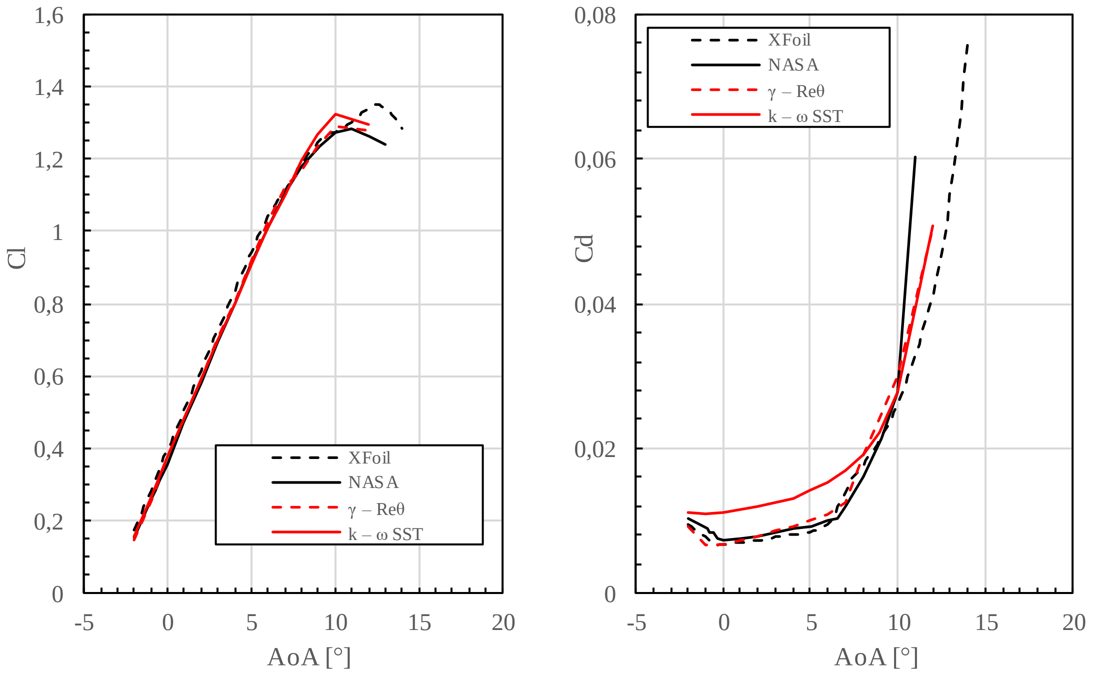

(a) Cl versus AoA, Re 4.6 x105

(b) Cd versus AoA, Re 4.6 x105

Figure 4.2: E387 lift and drag coefficients results from STAR-CCM+, XFOIL and Wind-tunnel experiments

The results from the $k - \omega$ SST model without the transition add-on may be explained due to the nature of the model itself. As summarised in *4.2.1 SST $k - \omega$ Turbulence Model*, the model developed by Menter is specific for when turbulence is known to be present and develops near the leading edge. That does not seem to be the case in this simulation since the transition model depicts a laminar behaviour until some extent on the profile surface. So, if the turbulence model determines that transition is occurring near the leading edge, the drag component from the turbulent kinetic energy, which extends at full length on the suction side, may add the extra percentage that is seen at the results. That turbulent behaviour will be seen next.

Figure 4.3 represents the intermittency factor and Figure 4.4 and Figure 4.5 the turbulent kinetic energy, for the E387 aerofoil at an angle of attack of 4°. The intermittency factor shows the probability at a given time and space of the flow to be turbulent or laminar, where red represents turbulent flow and blue laminar flow. When the flow closes to the hydrofoil wall, the intermittency near the wall is zero: the flow does not have the probability to be turbulent. However, that changes around half of the hydrofoil, where the flow will have a turbulent fashion (intermittency of 1). The negative velocity in i direction is also plotted in grey scale but is so small in the pictures it becomes hard to spot. Despite that, this may be the best indicator of a laminar separation bubble (LSB), because, like covered on 2.7 *Boundary Layer*, due to the adverse pressure gradient, the flow will tend to circulate backwards near the wall and again on the initial flow direction when it touches the upper flow layers. The intermittency value of near 0 at that area credits this theory, as also anticipated in Case Study 1. The length of the LSB is around 16%

of the chord, categorising it as a short bubble [24], and its thickness of 1 % (double of the value measured since the vector only shows the backward circulation). Finally, Figure 4.4 verifies the above, where the turbulent kinetic energy has a peak about the end of the LSB, signalling the reattachment of the flow to the turbulent boundary layer. These effects are observed throughout different AoA's.

On Figure 4.5 is proved that the $k - \omega$ SST model predicts the flow separation sooner than the transition model. No LSB is present on the results from this model.

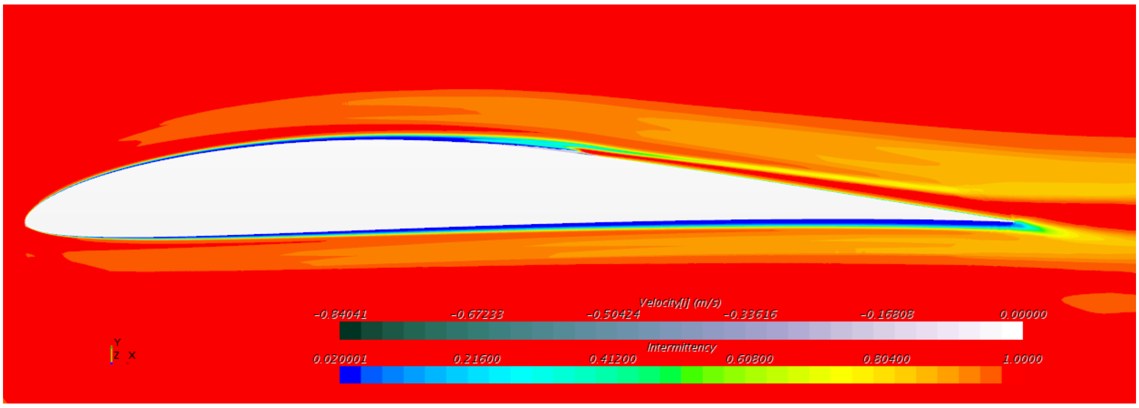

Figure 4.3: Intermittency for the aerofoil E387, AoA 4°, k – ω *SST* $\gamma - Re_\theta$

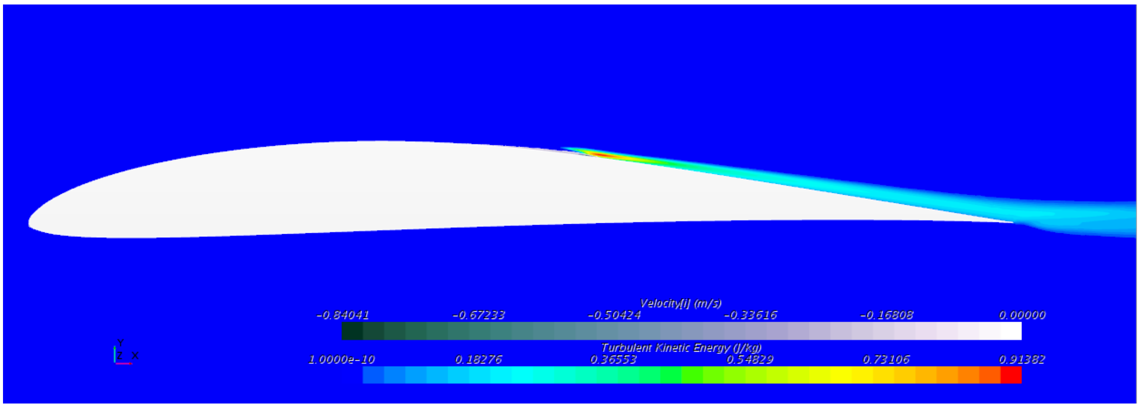

Figure 4.4: Turbulent Kinetic Energy for the aerofoil E387, AoA 4°, k – ω *SST* $\gamma - Re_\theta$

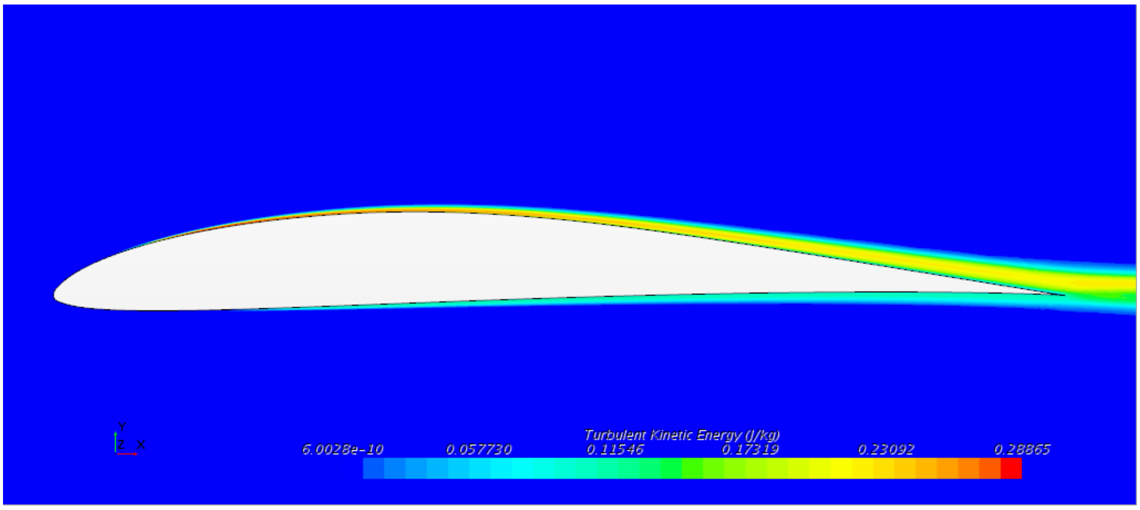

Figure 4.5: Turbulent Kinetic Energy for the aerofoil E387, AoA 4°, k – ω *SST*

Using the visual tools from Star-CCM+, an estimate of the transition location is presented in Figure 4.6. No model gives an exact location for this phenomenon, so the measure is done by verifying the peak in turbulent kinetic energy, near the hydrofoil wall. On this analysis, only the results from the $\gamma - Re_\theta$ model are used. Any measurements from the $k - \omega$ SST model would not contemplate the transition effects and flow reattachment. The results are compared to the XFOIL data.

Reading the Figure 4.6, Star-CCM+ predicts a later transition on the suction side, and an earlier transition on the pressure side, comparatively to the XFOIL results. Some factors may be the underlying cause of these inconsistencies. For example, XFOIL predicts transition but not recirculation, as of its nature. It has been seen that recirculation is occurring on this case. Also, on XFOIL the geometry was obtained using the coordinates from the website *Airfoil Tools*. These coordinates would prove insufficient to create panels, panels that would model the surface. Thus, the command `PANE` was used to multiply the number of panels. This may have deformed the geometry slightly, resulting on different values from Star-CCM+. For the later, the approach was different, as it begun with the same coordinates, but a special spline was fitted using the tools available on Rhinoceros 3-D software. This created a smooth surface, with no vertices subsequent from planes. Even the initial flow configurations on XFOIL, which were left as original, may have influence. As for Star-CCM+, the values regarding freestream turbulence intensity and turbulent length scale may not be the most appropriate or alter the final results. The mesh may also cause perturbations on the transition point if it is not adequately refined. However, as wall Y^+ factor was kept in consideration along with the simulations, and compels the mesh to be conveniently refined, it is unlikely to be the problem.

Finally, the pressure distribution is plotted for the AoA of 0° (Figure 4.7). The results from Star-CCM+ follow the same fashion as the XFOIL data, although less accurately on the suction side. The pressure coefficient seems higher on the suction side, and the pressure leap, due to the separation, also comes slightly after. On the wind-tunnel results, possibly due to the low amount of sample points, the pressure has the same magnitude but much less definition on the leading edge and at the separation point.

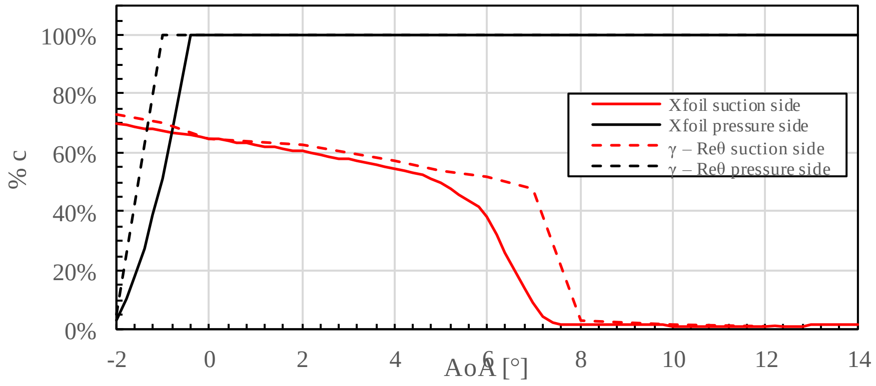

Figure 4.6: Transition curves for E387, XFOIL vs $k - \omega$ *SST +* $\gamma - Re_\theta$

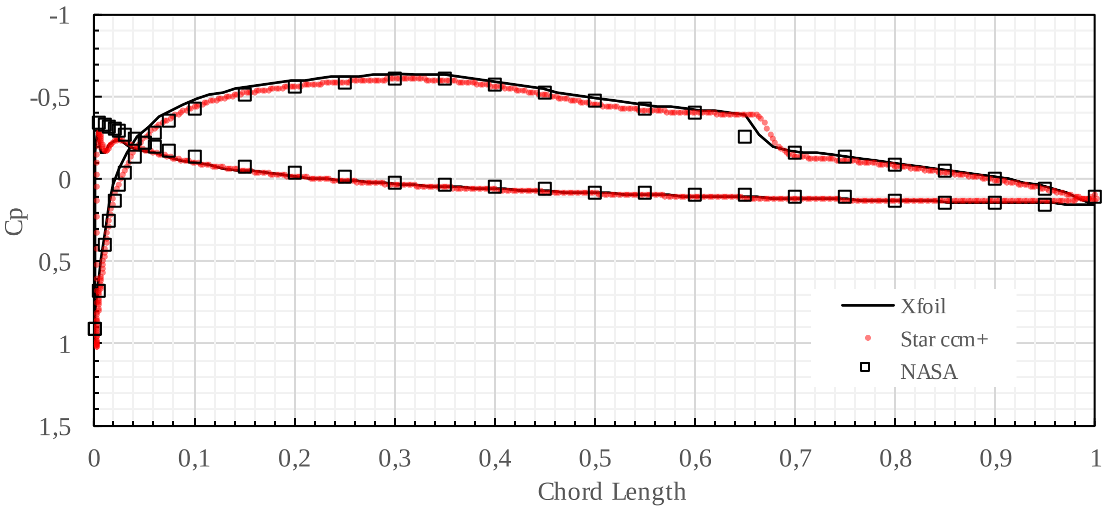

Figure 4.7: E387 pressure distribution, AoA 0°, k – ω *SST* $\gamma - Re_\theta$

4.5 Validation Conclusions

This chapter ends with a preview of the necessary models and instructions for the following chapters. The main two ingredients: the mesh parameters and the models and methodology on how to operate these models was verified here.

For the 2-D analysis, the mesh parameters will be the ones used in this chapter. The objective is to recreate as faithfully the conditions in all simulations.

The two models under the scope, the $k - \omega$ SST and its add-on $\gamma - Re_\theta$ model for transition were compared. The $k - \omega$ SST performs well for lift determination but fails for drag estimation. It is also uncapable of correctly estimating the transition point. The reasons to first consider this model was for the fact that the simulation residuals tend to converge fast, saving time and because the simulation could be turbulent since start.

On the other side, adding the transition model, the lift and drag coefficients are correctly estimated, and provide close values to the wind-tunnel tests. The transition can be estimated, although, without wind-tunnel data, it is impossible to say which of the tests performed (Star-CCM+ and XFOIL), is closer to reality.

That being said, the $\gamma - Re_\theta$ will be the only model to be applied on the next stages, as it is expected to estimate the lift and drag coefficients, transition and pressure closer to real experiments.

Chapter 5

SFWB Profile Performance

Following the validation done in Chapter 4, the present chapter will explore the behaviour of the fin profile using the previous conditions. The results are compared to the estimations made in Chapter 3, for case study 1.

5.1 Case Study 4: SFWB Results

Using the aerofoil from case study 1 after the repair, the simulation was replicated like *Chapter 4: Mesh, Turbulence and Transition*. The same mesh parameters and physics' models where used. For the velocity, only three flow speeds are employed and represent the expected low, mean and top speeds the fin will experience. This way, only simulations at the Re numbers of 2.5 $x10^5$, 5.0 $x10^5$ and 7.5 $x10^5$ (respectively 2.100, 5.250 and 7.875 m/s), where performed. The fin chord is of 100 mm (corresponding to the length at the root).

Regarding CFD simulation nature, the P113 profile behaves like the E387: no convergence is found when using the steady state solver. At the beginning of simulations, especially for larger angles of attack, vortexes could be seen before the simulation converged. When the residuals drop, this instability will disappear. One of the possibilities is for it to be Von Kármán vortex street, but, as simulations converge, it ceases to produce vortexes. Another option is Kelvin Helmholtz instability, which is characterised by a velocity difference, in this case, between the fluid and the fin interface. The velocity shear induces the formation of what looks like curls, and the initial, larger ones dissipate when the velocity stabilises. Near the wall may be occurring instability, which is so small it is hardly captured. This surface tension does not seem to have a significant interference in the lift, drag and pressure distribution. For example, for the Re of 7.5 $x10^5$, it is clear to see at 8 degrees (around when the foil stalls), that the variation of pressure and lift is approximately 10^{-3} (Figure 5.1, Figure 5.2 and Figure 5.3). This way, and since the first seconds into the simulation the field is not physical (breaks continuity laws), an unsteady solver is used, that in the end depicts a steady solution.

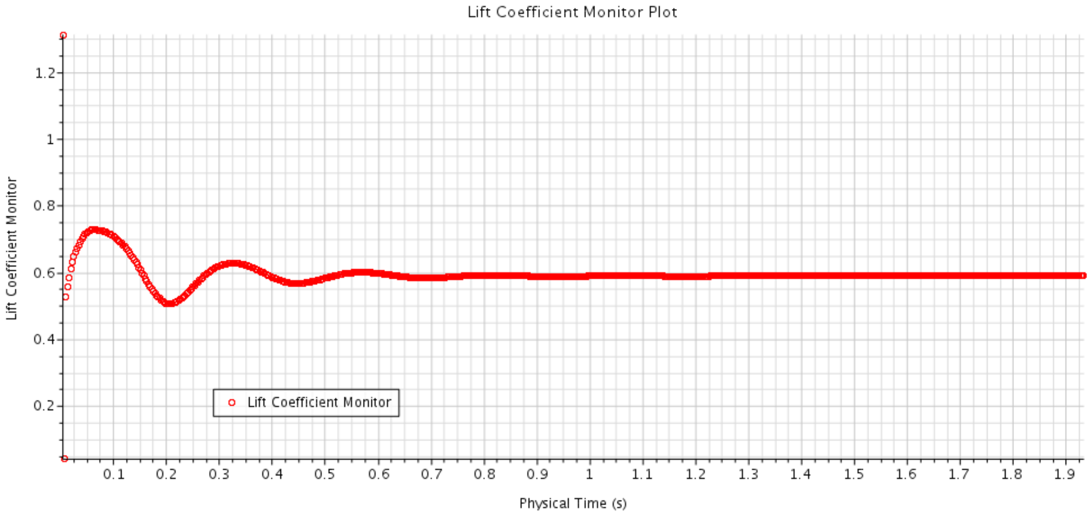

Figure 5.1: Lift coefficient monitor, Re 7.5 x10^5, 8° AoA

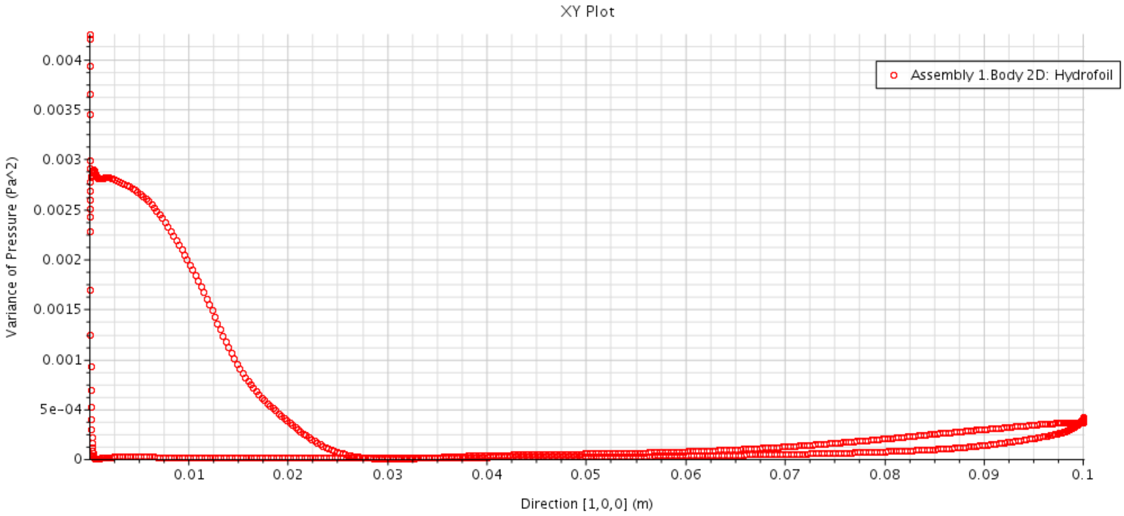

Figure 5.2: Variance of Pressure for the complete simulation, Re 7.5 x10^5, 8° AoA

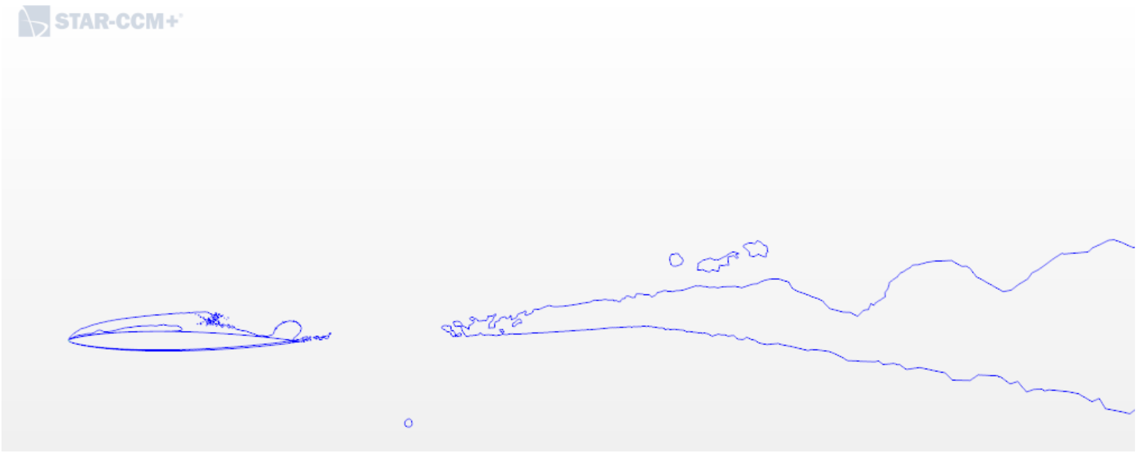

Figure 5.3: Q-Criterion for converged solution, Re 7.5 x10^5, 8° AoA

As Figure 5.1 shows, the lift coefficient tends to stabilise to a number with 5 decimals after 2 seconds. At this stage, the residuals are fully converged, leading to the belief that the solution is found. In Figure 5.2, the mean variance of the pressure along the profile is depicted. As expected, the variance is more significant near the leading edge, due to the fluctuation of the fluid and the point of separation. Also, of relevant value is the variance near the trailing edge, expected once turbulence will occur as the fluid leaves the pressure side of the foil. Parallelly, to help visualise the shape of the turbulent field, the Q-Criterion is shown in Figure 5.3. This scalar displays the LSB clearly at around 50 % of the hydrofoil, followed by a reattachment zone, and then evolving to turbulence.

Concerning transition, the results were taken in the same way as Chapter 4. The wall Y^+ was verified to be below 1, at the mesh generation stage, so case study 3 and 4 had to be done almost simultaneously to obtain a mesh that fitted both. Figure 5.4 below represents the transition curves from XFOIL and-Star CCM+, for a Reynolds number of 5 x10^5. The behaviour in both cases is alike, with Star-CCM+ predicting separation on the suction side somewhat earlier. That may be due to the way the measurement was done since no function with the used models provides the exact place for the transition.

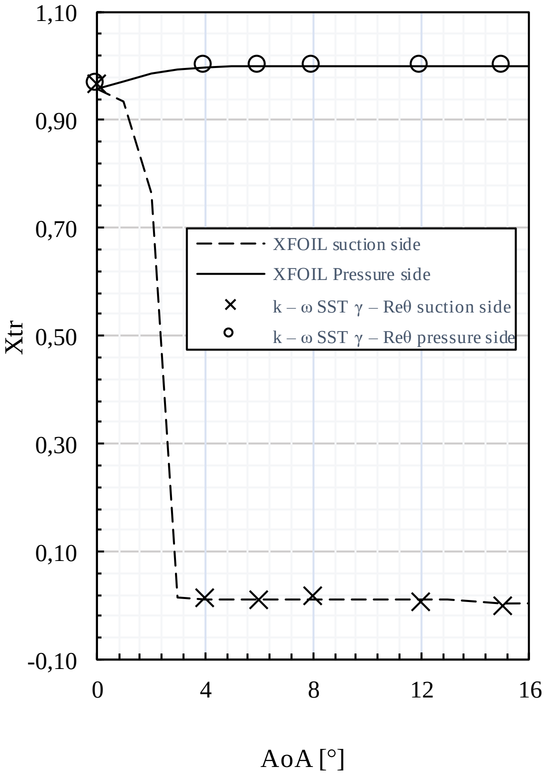

Figure 5.4: Transition curves for P113, XFOIL vs k – ω *SST + γ – Re*$_\theta$*, Re: 5 x*10^5

This transition behaviour is complemented with the formation of laminar separation bubbles. Taking the example of the simulations for Re 5 x10^5, it is seen the formation of twin bubbles, on suction and pressure side, at the trailing edge. This fits with the transition prediction results, which show transition at about 97 % (see Figure 5.5). As the angle of attack increases, the LSB shifts to the leading edge. Depending on the direction of the flow, the pressure side will always tend to have a full laminar flow around it. Three bubbles appear in Figure 5.6: one at the trailing edge on the pressure side, and two on the leading edge. The first one, on a), shows the flow is recirculating at the tip, but the outer layers of the flow remain laminar, as no turbulence is identified. For the leading edge, on b), the bubble seen at the pressure side is not an actual bubble but only a characteristic of the flow hitting the wall, stagnating and accelerating around it, on -*i* direction (Figure 5.7).

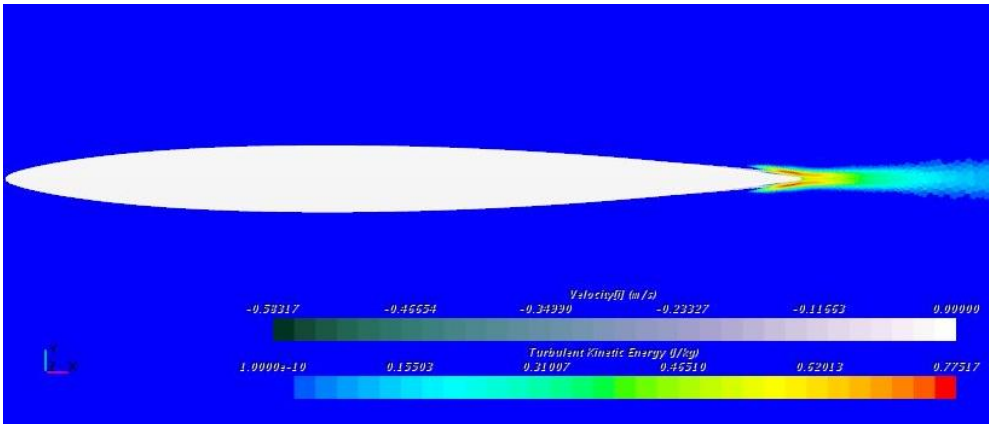

Figure 5.5: Turbulent Kinetic Energy for the hydrofoil P113, AoA 0°., Re: 5 x10^5, $\gamma - Re_\theta$

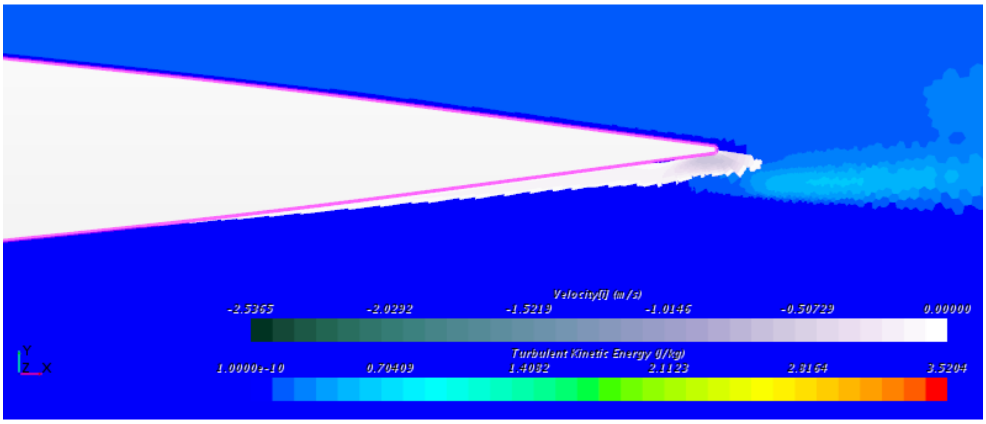

(a) Recirculation bubble at the trailing edge

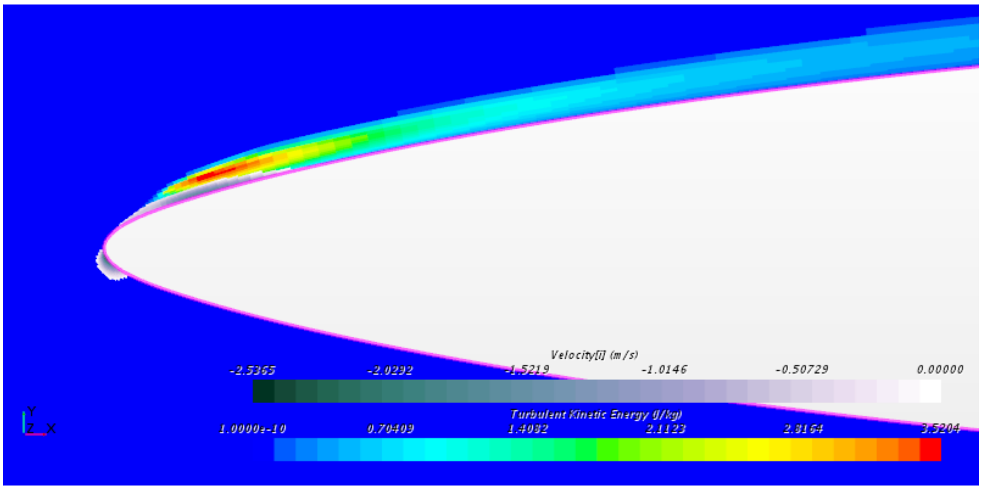

(b) Recirculation bubble at the leading edge plus stagnation point

Figure 5.6: Turbulent Kinetic Energy for the hydrofoil P113, AoA 4°., Re: 5 x10^5, $\gamma - Re_\theta$

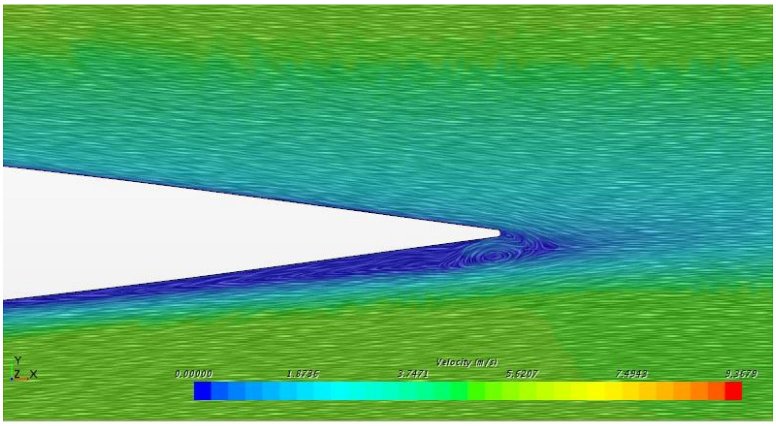

(a) Trailing edge recirculation bubble

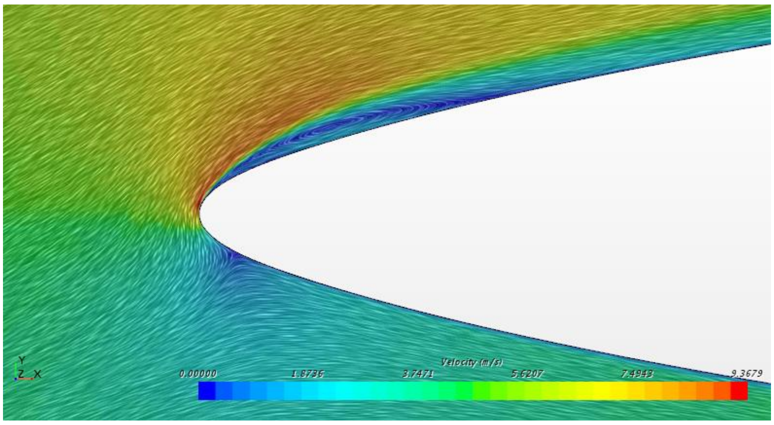

(b) Recirculation bubble at the leading edge plus stagnation point

Figure 5.7: Velocity vector line display for the hydrofoil P113, AoA 4°., Re: 5 x10^5, $\gamma - Re_\theta$

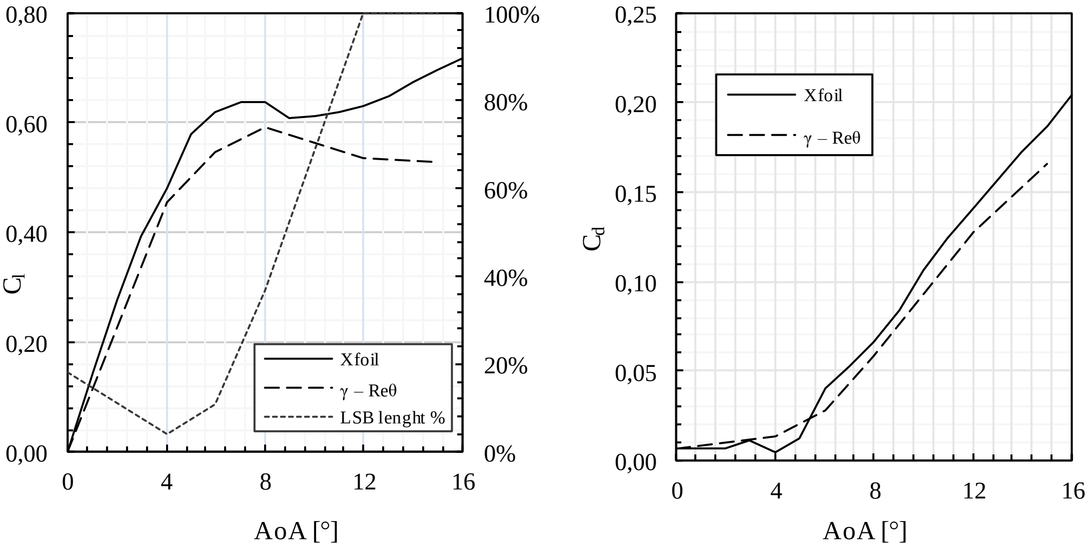

(a) C_l versus AoA and LSB length *(b) C_d versus AoA*

Figure 5.8: Lift coefficient and LSB length in chord percentage for AoA spectrum, Re: 5 x10^5, $\gamma - Re_\theta$

The actual laminar separation bubble is at the suction side and, at 4 degrees, measures about 4 % of the chord length. The size of the LSB increases consistently with the progression of the AoA's and proves essential for the stall of the profile as shown in Figure 5.8. This shows a direct dependence of the size of the bubble and the moment where the profile starts to lose lift. As seen, around 8 degrees, the size of the LSB is about 30 %. The lift coefficient drops at this point, as stall sets, this behaviour predicted at the experiments from Lissaman P. [28]. Before, as the LSB starts to grow, the slope of the C_l starts to drop, as expected.

The values for the lift and drag coefficient, on the previous Figure 5.8, much like case study 3, on Figure 4.2, show how the XFOIL and Star-CCM+ provide different results. For the lift coefficient, the obtained values are overall higher on the XFOIL simulation than the results provided on the Star-CCM+. The curve is also smoother, but that may be due to the number of samples. For the C_d, the situation is reversed: Star-CCM+ detects less drag than its counterpart. This may be due to the number of cells on Star versus the length of the panels on XFOIL. The orientation of the poor panelling distribution on XFOIL may be contributing to the increase of area in the way of the flow, making this coefficient rise. All these results are expected since XFOIL has limitations on transition.

Because on the first seconds into the simulations, the foil induces a significant disturbance in the flow, a detailed analysis of the pressure has been done. This comprehends the analysis of the values' flotation, on each cell around the hydrofoil wall, and the calculation of the mean value from a set of measurements. The results from this study show that, after the residuals are converged, the pressure flotation is less than 1 Pa, which may be neglected comparing to the value order, 10^{-3}. This way, a graph comparing the Star-CCM+ and XFOIL results is plotted, showing the pressure around the foil (Figure 5.9). The most visible distinctions are on the leading edge on the suction side. Although the module value is very similar at the tip, the pressure distribution after behaves distinctively. There is a pressure rise after the tip, with a small plateau, and after approximately 10 % of the chord, the pressure registered on Star-CCM+ is higher than the one delivered by XFOIL. The first difference may be explained by the nature of the transition model, which may be giving fine details and simulating the laminar separation bubble, hence the pressure rises, or could as well be the increase of cells in the mesh compared to the number of panels for the XFOIL. As for the second part, the reattachment of the turbulent boundary layer may be influencing the results, which would not be captured on XFOIL. At the pressure side, since no bubbles or other transition singularities are expected, the results are relatively the same.

Finally, interestingly, still, for 4 degrees simulation, there seems to be a boundary layer where the flow as equal chance to be laminar or turbulent (in Figure 5.10, as seen with the intermittency scalar). This boundary layer forms above the viscous layer and the turbulent reattached boundary layer, caused by the leading-edge separation bubble and holds until the end of the profile. This favours the idea of an LSB, with linear flow above it.

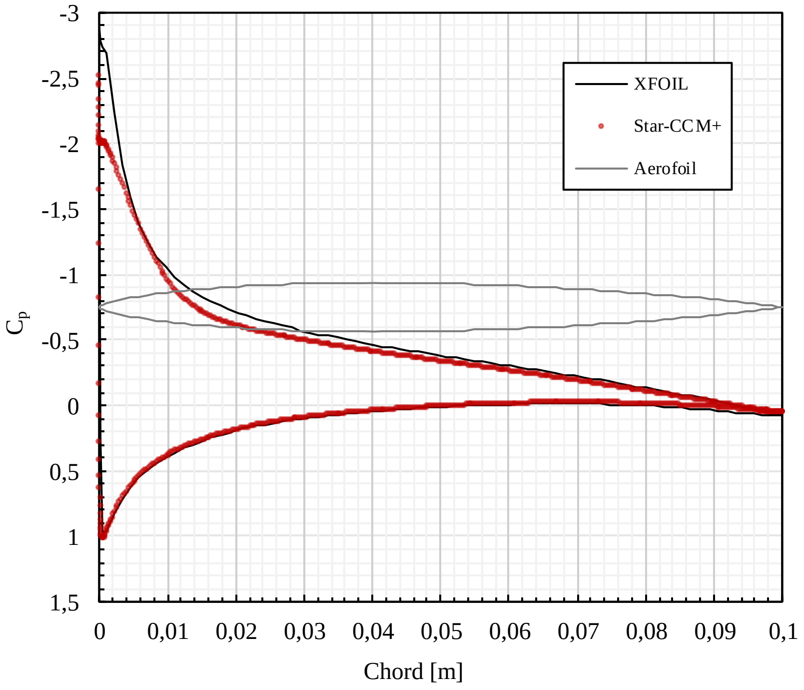

Figure 5.9: Pressure Coefficient for the hydrofoil P113, AoA 4°, $\gamma - Re_\theta$

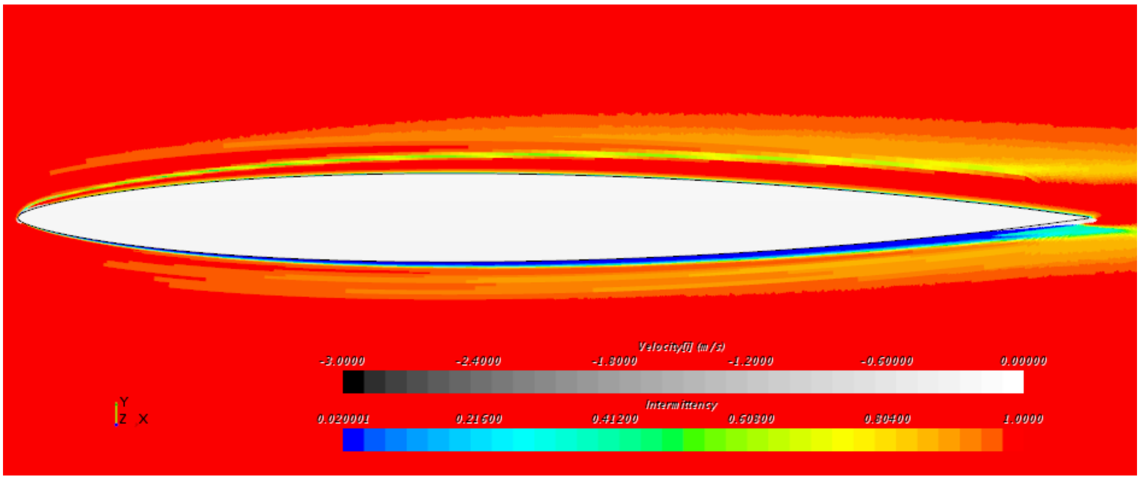

Figure 5.10: Intermittency for the hydrofoil P113, AoA 4°, $\gamma - Re_\theta$

5.2 Mesh Convergence Study

In order to prepare the next chapter regarding the 3-D fin study, a mesh convergence study was performed. This study will provide the mesh size that inputs a 5 % to 10 % error in the results. The characteristics are the 5 x10^5 Re and 8 degrees of angle of attack. The lift and drag coefficient will be the parameters to be analysed.

The study began with the previously used mesh and evolved to a lesser number of cells. The parameters adjusted were the control volumes cell size. Table 5.1 compiles all the seven different mesh sizes and respective results. All the studies complied with the wall Y^+ factor smaller than 1. Mf represents the initial mesh, and on the following numbers, the mesh becomes coarser.

Table 5.1: SFWB two-dimensional mesh parameters

	Mf	**M1**	**M2**	**M3**	**M4**	**M5**	**M6**	**M7**
Base Size [m]	0.5	0.5	0.5	0.5	0.5	0.5	0.5	0.5
Number of Prim Layers	30	30	30	30	30	30	30	30
P. Layer Stretching	1.15	1.15	1.15	1.15	1.15	1.15	1.15	1.15
P. Layer Thickness [m]	0.005	0.005	0.005	0.005	0.005	0.005	0.005	0.005
Surface Growth Rate	1.08	1.08	1.08	1.08	1.08	1.08	1.08	1.08
V1.0 Costume Size [m]	0.001	0.0015	0.002	0.003	0.004	0.006	0.008	0.010
V2.0 Costume Size [m]	2.8 x10^{-4}	3.0 x10^{-4}	3.5 x10^{-4}	4.0 x10^{-4}	4.5 x10^{-4}	5.5 x10^{-4}	7.0 x10^{-4}	0.001
V3.0 Costume Size [m]	3.2 x10^{-5}	3.5 x10^{-5}	4.0 x10^{-5}	4.5 x10^{-5}	5.0 x10^{-5}	8.0 x10^{-5}	1.2 x10^{-4}	5.0 x10^{-4}
C_l difference [%]	-	0%	0%	0%	1%	1%	1%	1%
C_d difference [%]	-	0%	1%	2%	2%	3%	4%	7%
Number of Cells	108224	80230	62135	48938	42212	32683	25382	17583

To decide on the best mesh to proceed with, the same physical models from the previous case studies 3 and 4 were used. The simulations start from the implicitly unsteady state, 2nd order, and at a time step of 0.01 and 60 iterations. This method provides quick and full convergence of the residuals for the first 3 studies. For the remaining, the time step and the number of iterations per time step had to be increased, being around 0.001 and 80, respectively, to obtain converged values. This increased the computation time.

The last mesh, M7, goes out of the scope for having a difference in a drag coefficient of 7 % to the finer mesh. It is noticeable that the drag coefficient is also the most delicate factor on the study, perhaps because it is measured in the *i* direction, and this is where the number of cells is more substantially reduced. By other words, the number of cells transversely to the foil is significantly inferior to the number of cells longitudinally, so, increasing the cell size will make the number of cells decrease, thus resulting on a worse result.

So, the mesh parameters to be used are the ones with a lesser number of cells but still inside the 5% error margin. M6 is a good candidate for further analysis, since the low number of cells, 23.5% of the original value, promises to shorten the computation time.

Figure 5.11 shows how the Cl and Cd results obtained for each mesh may fluctuate around a polynomial a 3rd and 2nd order function. The outliers where kept but should be disregarded.

It needs to be taken into account that having a less refined mesh will improve computational time but on the other side, takes a levy in the results.

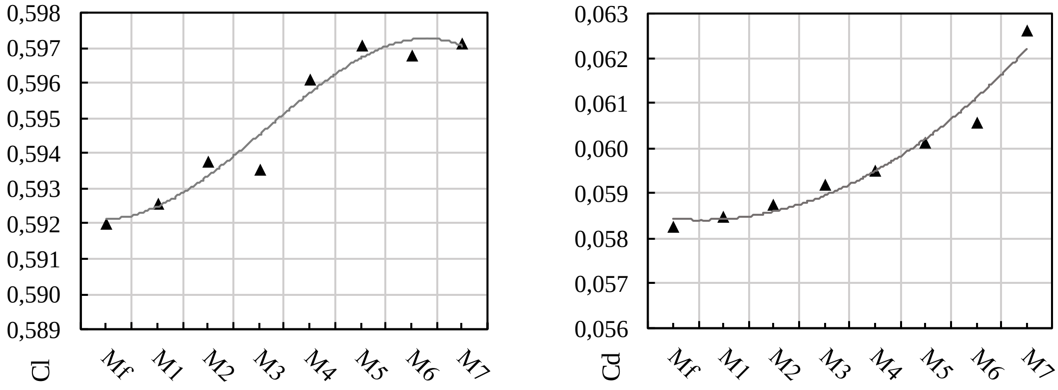

Figure 5.11: results for Cl and Cd for different meshes

5.3 General Conclusions

The present chapter aimed at characterising the flow around the hydrofoil. This characterisation understood not only the usual coefficients, like lift, drag and pressure but also the intrinsic features developed by its geometry. The work was made easier due to the previous chapter, that opened the way for the best mesh and physical model parameters, that work fit for the required velocity window.

There were three simulation sets, for the three velocities, despite only Re 5 x10^5 is shown. The remaining tests are for other ongoing investigations, that require the approximate value for the pressure at the SFWB.

To have a better equivalence between case 4 and the previous case 3, the two meshes were developed simultaneously. This way, the wall Y^+ factor could be coordinated, and both meshes made with parameters that would fit E387 and P113 profiles.

The best model for this case was the $\gamma - Re_\theta$, that was run with an implicitly unsteady solver (step between 0.01 and 0.001), and 20 to 80 iterations per time step, depending on the velocity and angle of attack. The presence of laminar separation bubbles is guaranteed, and these govern the behaviour of the flow and the coefficients. The bubble increases size as the angle of attack rises until the flow entirely separates from the suction side and only a massive recirculation bubble is left covering all lower pressure surface.

Considerable concern was given to the pressure values, as they are the material need for another ongoing thesis. These values would be calculated via the mean value, and the extreme values evaluated. Once the vortex phenomena disappear, the values of pressure stabilise and assumed to be stationary.

Chapter 6

SFWB Operation

As a final step to understand the flow behaviour, the simulations took the final step. In this chapter, the conditions used in Chapter 5 will be summoned to create a 3-D fin simulation. Only one velocity and angle of attack case will be investigated on this thesis, although more cases are under study. The fin, the initial reference for the 2-D geometry that had to be fair, was not changed and represents the piece as the maker first crafted.

6.1 Physical models and mesh considerations

Concerning the physics models, they are the same as used before. This way, there will be the $k - \omega$ SST turbulence model with the add-on of $\gamma - Re_\theta$.

In what relates to the mesh, efforts were made to have a close mesh to the one used in Chapter 4 and Chapter 5.

On the previous studies, all the control volumes are rectangular, as the section was only used on a 2-D study. For the 3-D analysis, it is essential to have in mind that the fin has different configurations in its length. That means that, if a prismatic control volume is fitted, the distance between its interface and the fin surface is changing in the z-direction. The cell size will be small in areas where there is no interest in having small cells and only adds to the simulation time. That is especially true for the V3, that has the smaller cell size. At first, the control volume V3 was designed to cover only the leading and trailing edge, like on the 2-D simulation. To simplify that model, the next idea was to have a fin 20 % larger to be the control volume, guaranteeing a small mesh size along all the surface. That operation proved to be unreliable, as the number of cells would exceed 100M and the program crash. Thus, simulations were performed using V1 and V2 with sizes on table 6.1 and configuration on Figure 6.1. V3 is not considered on this analysis.

When producing the 3-D meshes using the M6 parameters from Chapter 5.2, the M6 took around two hours with an Intel(R)Xeon(R) CPU E5-2650 v2 @ 2.60GHz with 158 GB RAM, generating 11M cells.

In the subject of simulations, these start at 0 degrees of AoA and are run in a steady state for around 100 iterations. After the solver is switched to implicitly unsteady, and the residuals made converge. This is done by tuning the time-step and the number of inner iterations. When convergence is attained, and without changing any previous settings, the AoA is changed. If not needed, no further changes are made to the time step and number of inner iterations.

Table 6.1: domain and control volumes' dimensions for 3-D solution

Name	**Width [mm]**	**Height [mm]**	**Depth [mm]**
Domain	2000	1500	725
V1	300	100	400
V2	120	200	400

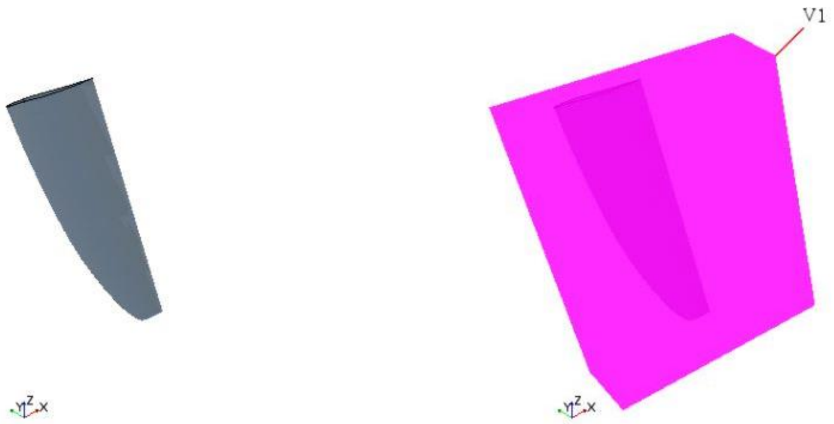

(a) Fin (b) V1

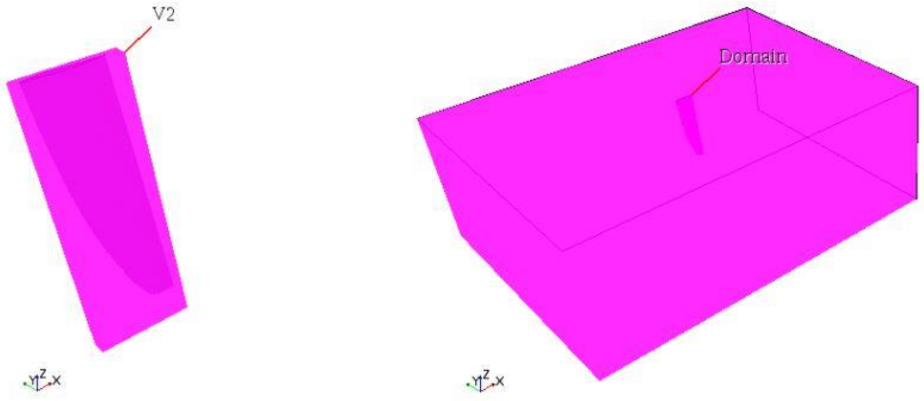

(c) V2 (d) Global Volume

Figure 6.1: 3-D Control Volumes

6.2 SWBD Three-Dimensional Aerodynamic Analysis

As stated at the beginning of this chapter, only one case, meaning one angle of attack at one velocity regime will be under the scope. This case is at Reynolds 5.0 x10^5 and 0° of AoA. The remaining cases will be characterised on future work.

In what concerns the laminar separation bubble, the results from the 2-D analysis show a bubble on both sides, near the trailing edge, covering about 18 % of the surface. For the 3-D study, the scenario is similar, having a proportional LSB along three-quarters of the fin and covering 18% of the chord, and a narrower bubble near the tip (Figure 6.2). This bubble fades and disappears at the tip, while near the board surface it is inexistent, due to the boundary layer. It is expected that the LSB will increase chordwise on the suction side while translating towards the leading edge. These results are to be verified in future work. It will also be verified if, after 8 degrees, the bubble bursts and all the flow become turbulent.

Also, will also be peremptory to determine the lift and drag coefficients, and values have the AoA increases. As the results from Chapter 5 suggest, the foil should stall after 8°, typically 2 to 3 degrees after the 2-D analysis results. This will also be asserted or refuted in the future.

Figure 6.2: LSB at the Fin, Re: 5.0 x10^5, 0° AoA

Concerning the pressure distribution, a plot was obtained for the planes captured on Chapter 3.3 (see Figure 6.3). The suction and pressure symmetric sides are overlapped and, thus, only one curve for each section is depicted. These curves confirm the previous statement, in Chapter 3, that similar results are found in all sections. These are only scaled and have different Re numbers. Result wise; the curves illustrate the same particularities as the initial results from Chapter 3.3.1. It is clear the small pressure increase near the leading edge, a characteristic of the fin foil. The three curves have approximately the same magnitude, indicative of a constant flow velocity span wise.

Figure 6.4 compares the pressure results from Chapter 5 and the first curve from Figure 6.3, which are located at the same section of the fin (z =100 mm). Like previously, the most distinguishable characteristics is the step on the pressure near the leading edge. Also, as the Figure now uncovers, there are also differences on the trailing edge pressure. This may be different owed to the adaptation from 3-D to 2-D, which mandated a treatment on the trailing edge, due to the discretisation of the surface. When extracting the coordinates for the 2-D hydrofoil, a gap was formed at the trailing edge, that was then closed with a semicircle. Another possibility is the mesh size. The mesh size on the 2-D analysis is more refined than the mesh on the 3-D, the later resultant of a mesh conversion study, and, additionally, the third control volume was not included. Other than that, the results are coincident.

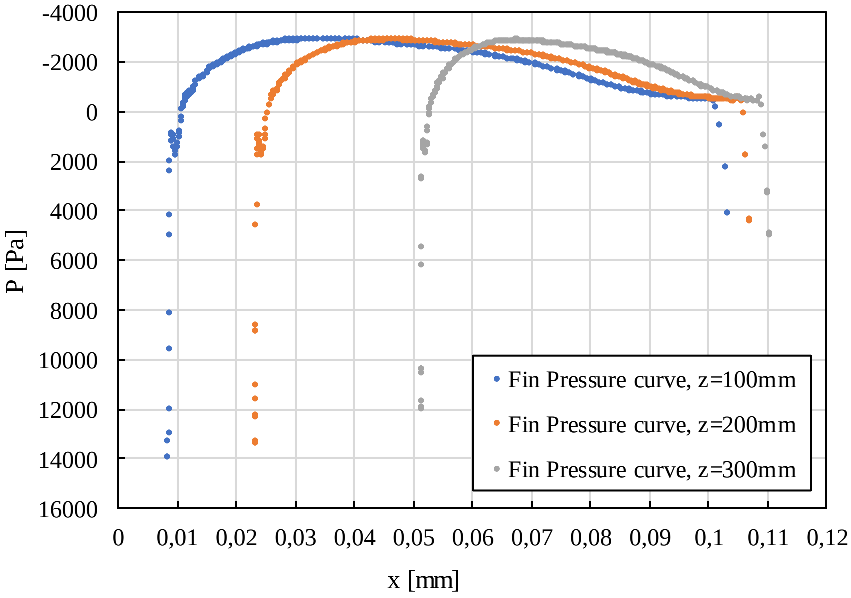

Figure 6.3: Fin Ox Pressure curves for AoA = 0°

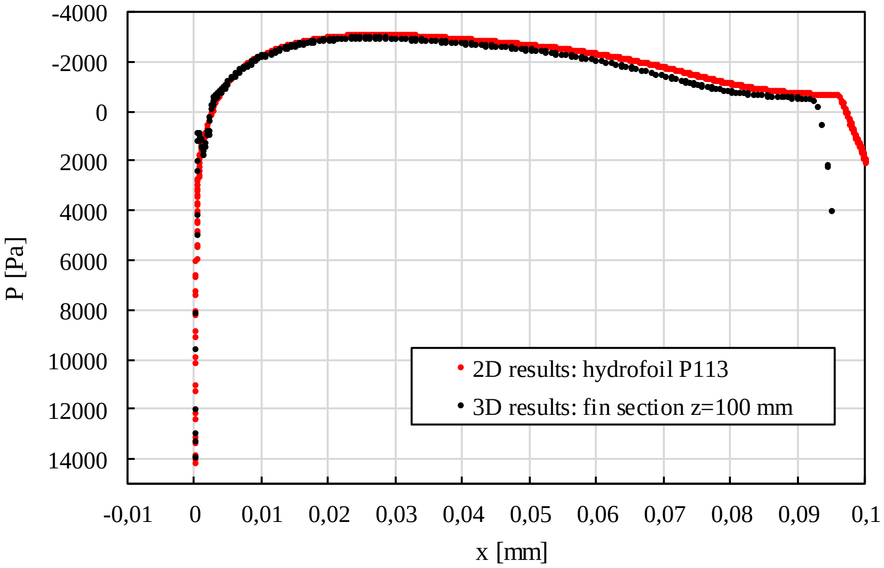

Figure 6.4: Comparison between 2-D and 3-D results: Pressure

Another interesting occurrence to verify is how the flow behaves after passing the recirculation bubble. After the flow recirculates, in theory, it should reattach as a turbulent boundary layer. Although in the previous chapter this phenomenon is more noticeable for higher AoA's, it is still included in the analysis. It is expected a small band just after the LSB and at the point where in Figure 6.3 the pressure increases, near the trailing edge. Confronting Figure 6.5 to these suppositions proves that they do occur, as the red band symbolises the LSB and the blue band the turbulent kinetic energy, a signal for turbulent flow. It is also curious to notice the collar around the fin and the plane where the fin fits the board. At this place, the mixture between the two perpendicular flows, the one on plane xOy for the board, and the one on xOz for the fin creates a zone of turbulence. Moving down in Z, it is seen that the TKE isosurface extinguishes, only to reappear at the fin tip.

In Figure 6.6 it is essential to state the higher values of skin friction at the leading edge, and also a small and thin band close to the trailing edge. This band, best visible near the fin attachment to the board, is the line where the flow is reattaching as a turbulent boundary layer. It is also seen higher friction values at the collar, at the same place where in Figure 6.5 is found the TKE blue band.

In Figure 6.7 are shown the streamlines. These lines are smooth and show no signs of turbulence or vorticity, although that is expected for the 0° AoA. For higher AoA's will be expected the formation of a spiral vortex at the foil tip. The blue colour on the streamlines indicates that the flow decelerates, represented at the leading edge (the stagnated flow), and at the final half of the fin, close to the trailing part. It is in balance with the pressure solution from Figure 6.3.

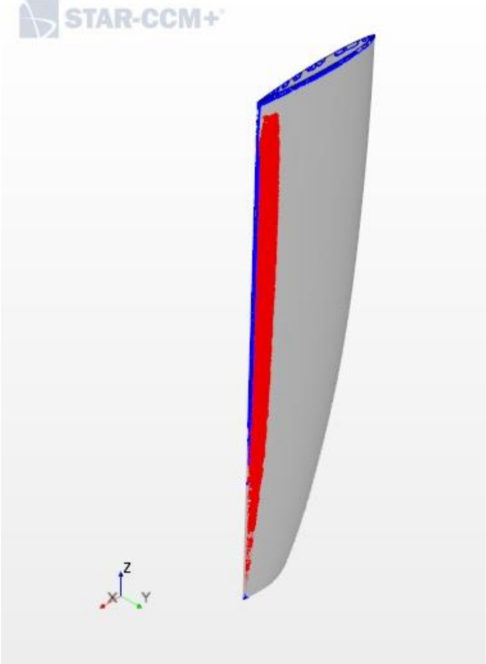

Figure 6.5: Turbulent Kinetic Energy (blue) and LSB (red)

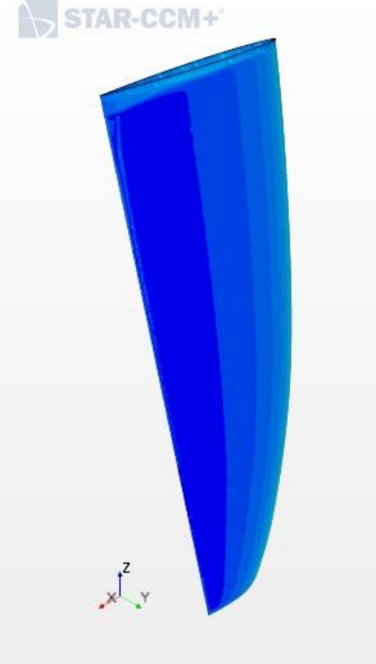

Figure 6.6: Skin Friction (gradient)

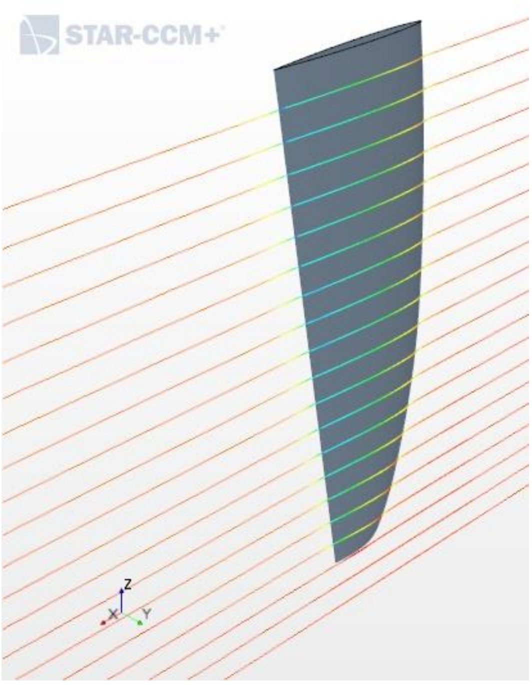

Figure 6.7: Streamlines at 0° AoA

6.3 General SFWB Conclusions

This chapter is the product of the development of the previous three chapters, namely 3, 4 and 5. It contains the results of the previous studies for the most suitable physics model, as well as the result of the mesh convergence study. With all the previous notes and prescriptions, the creation of a 3-D analysis was direct and straightforward.

As in prior chapters, an aerodynamic analysis was carried, to describe the SFWB behaviour when being used. Currently, only one angle of attack for one Reynolds number is described in this chapter. As part of the future work, more simulations will be done to cover the different AoA's at which the fin typically operates. In this chapter, it became clear that the flow is not fully laminar along the fin but has a transient behaviour.

These results are in line with the conclusions from Chapter 5. Along the fin surface, the velocity vectors closer and parallel to the wall change to an opposite direction of the flow. At that point, the flow separates, and an LSB is formed. In this case, it is seen to adhere back to the surface, but as a turbulent boundary layer, a more expressive sized sheet, as shown in Figure 6.5.

The comparison of the fin pressure distribution at z = 100 mm (Figure 6.4), seems to imply a loss of quality on the trailing edge. The coarser mesh and/or the lack of a more refined mesh at the edges of the fin may be cause to this; it may also be an intrinsic characteristic of the SFWB. Further research would need to be conducted to assess the result.

The turbulent kinetic energy at the fin tip (as seen in Figure 6.5), seems to promise increased turbulence at that place, after an increase of the AoA.

Chapter 7

Additional Studies

To complete the analysis, a series of individual studies were made. The first one, a parametric optimisation study, aims at understanding how the change in a small percentage of the hydrofoil definition may induce or not, a change in the flow.

Following, the next study represents how much would be the fin pressure loads from three user types: a beginner, a typical and an expert windsurfer.

Finally, with an understanding from Newcastle University, the data obtained from water tunnel experiments and CFD analysis will be, as possible, compared.

7.1 Parametric Optimisation Study

For the first study, the XFOIL tool was once more used, making this analysis 2-D. All modifications have been achieved using the program functionalities. In sum, the variations were applied inside the GDES menu, with the following commands:

`HIGH rr` Move camber and thickness highpoints

`TSET rr` Set new thickness and camber

The modifications described next are upon the actual thickness and position on maximum thickness. That means that a parameter variation will be 5 % of the total parameter value and not 5% of the chord. Since the profile is symmetric and thus no camber, this study was not included. The study compares the results for the Reynolds number of 5 x10^5, before and after modification.

7.1.1 5% Thickness Variation

The first modification concerns the maximum thickness variation. The values refer to the absolute maximum thickness. In chord percentage are 8.244 ±0.4122 % of chord length. Running the new hydrofoil in the same conditions as the previous runs in Chapter 3, returned the results on Figure 7.1 and Figure 7.2:

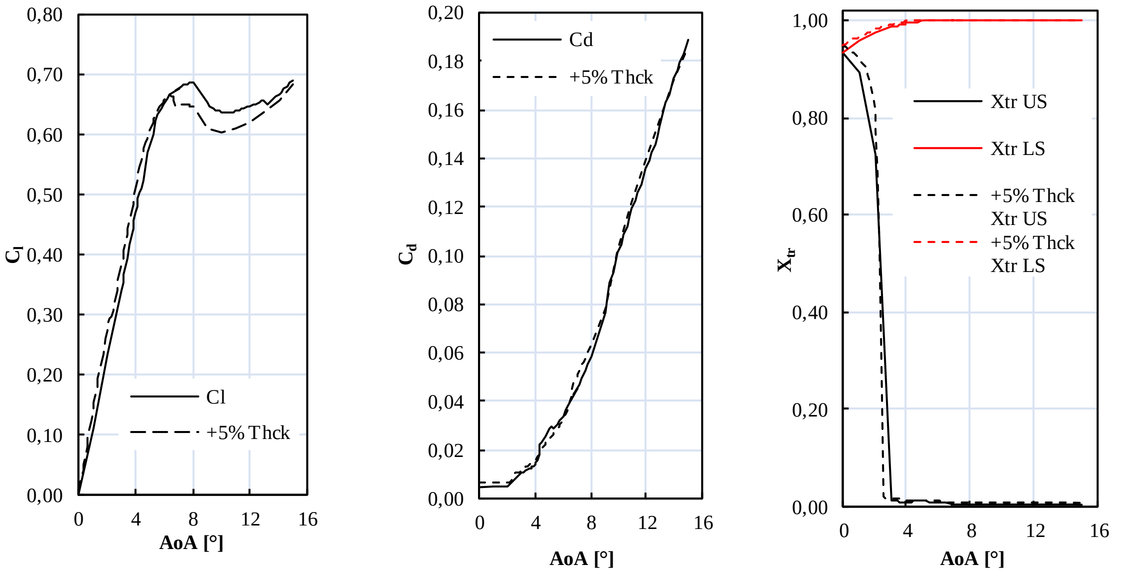

(a) Cl vs AoA for original profile and +5% thickness modification

(b) Cd vs AoA for original profile and +5% thickness modification

(c) Transition vs AoA for original profile and +5% thickness modification

Figure 7.1: Results for +5% thickness modification

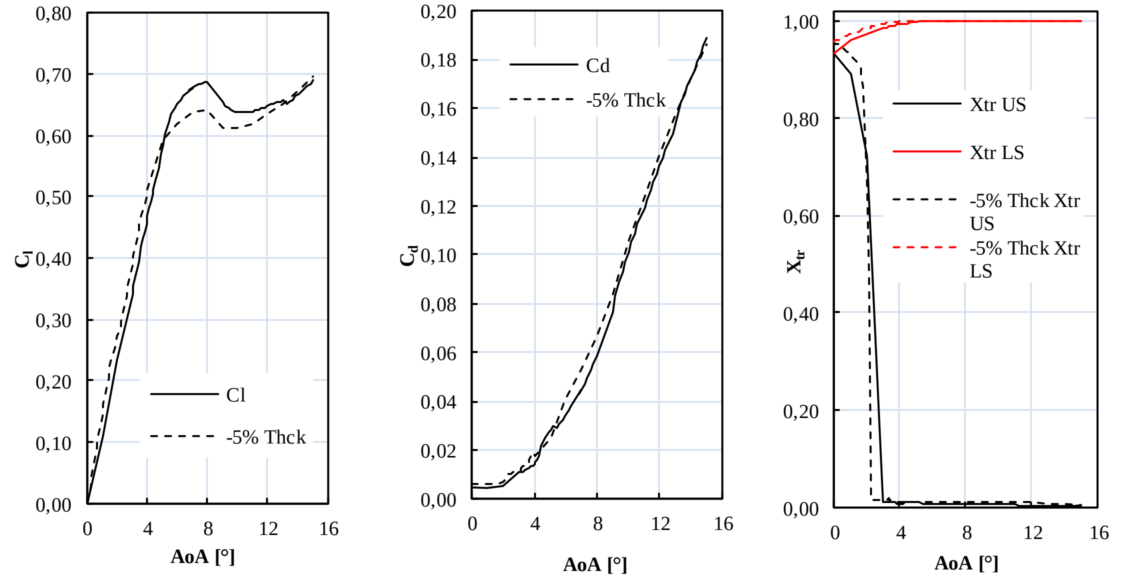

(a) Cl vs AoA for original profile and -5% thickness modification

b) Cd vs AoA for original profile and -5% thickness modification

c) Transition vs AoA for original profile and -5% thickness modification

Figure 7.2: Results for -5% thickness modification

The differences are minimal in the two cases. It is mainly seen that:

- The C_l (a) is higher in the linear region for the new cases (around 15% more), but also tends to stall before, at around a 6% lower C_l for 8 degrees;
- For the C_d (b), the +5% thickness case shows a very similar behaviour, while the decreased thickness case is showing more drag (about 10% between 5 to 9 degrees);

- Regarding the point of separation (c), almost no difference is felt on the lower side (LS), but, for small angles of attack, the flow is separating later. For the upper side (US), the separation point will move to the leading edge around 2 degrees, against the 3° as on the previous analysis.

7.1.2 Maximum Thickness Position Variation

Similarly, one can verify the effects of the position of maximum thickness. This position is achieved longitudinally, or along the chord, either 5% less than the original value or 5% more than it. This can be translated on the next Figure 7.3 and Figure 7.4:
The results look very similar to the previous ones. Most remarkably:

- In Figure 7.3 (a) stall is occurring about 12% earlier (for 7 degrees). Also of note the duality of solutions on this picture, due to two distinct convergence paths, one coming from lower angles of attack and another from higher angles. An occurrence already detailed on Chapter 3.
- The significant difference for the previous plots is in Figure 7.4 (c), where the separation is taking place at the same AoA, on the upper surface. There is still the gain for lower angles, where separation is happening further on the chord.

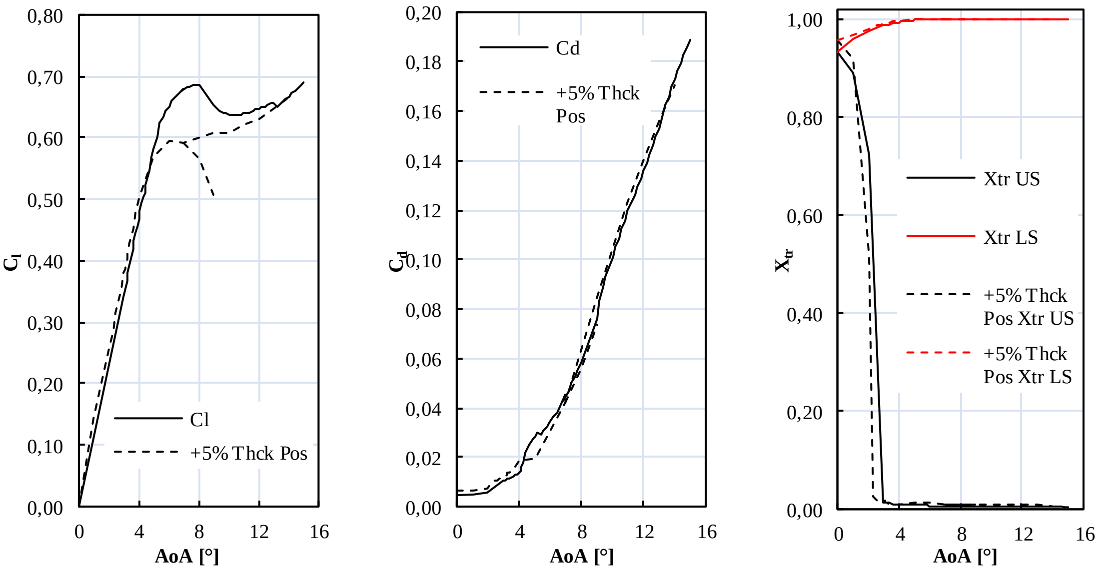

(a) Cl vs AoA for original profile and +5% thickness max position modification

(b) Cd vs AoA for original profile and +5% thickness max position modification

(c) Transition vs AoA for original profile and +5% thickness max position modification

Figure 7.3: Results for +5% thickness position modification

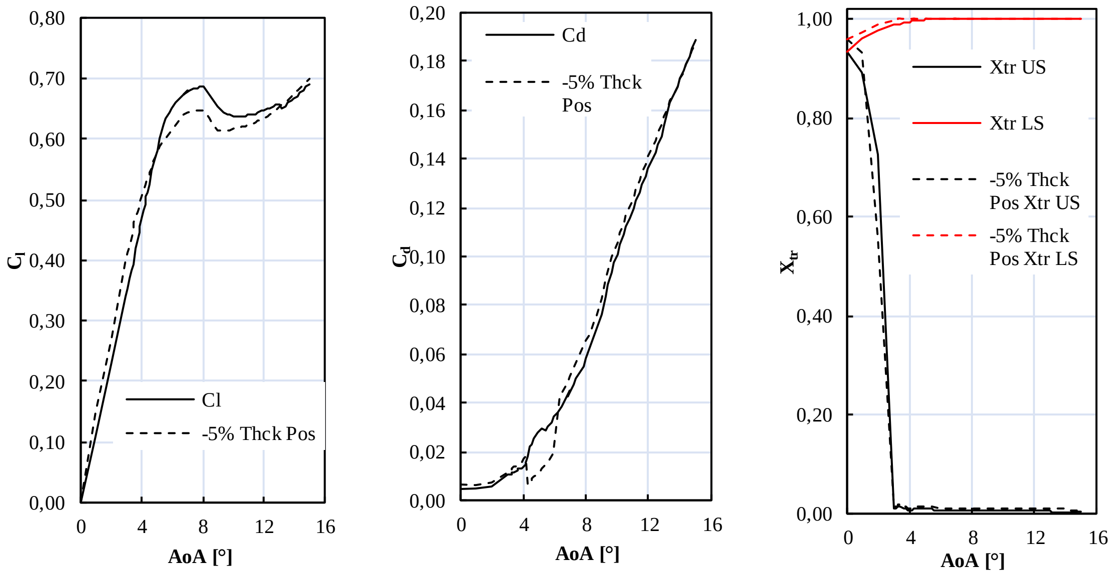

(a) Cl vs AoA for original profile and -5% thickness max position modification

b) Cd vs AoA for original profile and -5% thickness max position modification

(c) Transition vs AoA for original profile and -5% thickness max position modification

Figure 7.4: Results for -5% thickness position modification

7.1.3 Conclusions

This chapter proves that the variation of a small percentage of thickness is enough to change the fin behaviour. The lift coefficient performance changes for the worse in all cases. Unless it proves to be preferable to have such properties, it makes no sense to apply any of the modifications.

The same is true for the change in the maximum thickness position. The results show a more lift for small angles but an earlier stall, with an increase of drag and earlier separation of the flow.

This also shows that the fin needs to be very fine-tuned in what concerns its thickness, or the performance may be affected.

7.2 User Profiles

This chapter seeks to explore a visual and explicit way of telling by whom the SFWB should be used. This, together with a similar assessment for the ultimate strength, will show the stress gauge each user generates. The ultimate objective is to be able to verify the load applied to the fin and compare it to the maximum load, resulting in a user category label.

For that, three user profiles where created:

- **Basic User Profile**: intends to describe a beginner to the sport. This profile is characterised by sailing straight and at low speed, with the possibility of small manoeuvres.

- **Intermediate User Profile**: this user is more experienced than the Basic user so may achieve higher speeds. He is also able to perform some manoeuvres, in low and medium speed.
- **Master User Profile**: the master user typically sails at high speeds and is also able to perform manoeuvres.

To modulate the user profiles, a table was built (table 7.1). The idea behind it is that for each angle of attack plus velocity pressure is found. The pressure results are no more than the results obtained from Chapter 5. This pressure is the integration of all pressure measurements in all cells around the foil.

Then, another similar matrix is built for each user, but instead of pressure, as represented the probability of each event, or point in the matrix (table 7.2).

Table 7.1: Pressure values for velocity vs AoA

2-D	0°	4°	6°	8°	12°	15°
2.1 [$m.s^{-1}$]	0.178	0.319	0.397	0.443	0.494	0.498
5.25 [$m.s^{-1}$]	0.933	2.152	2.472	2.715	3.050	3.063
7.875 [$m.s^{-1}$]	1.840	4.838	5.521	6.057	6.828	6.849

Table 7.2: Event probability of an event for each user

v [$m.s^{-1}$]	**AoA [°]**	**USER 1 [Basic]**	**USER 2 [Intermediate]**	**USER 3 [Master]**
2.1	0	21.0%	6.0%	3.0%
2.1	4	18.0%	6.0%	2.0%
2.1	6	17.0%	9.0%	3.0%
2.1	8	10.5%	6.0%	4.0%
2.1	12	2.0%	2.0%	3.0%
2.1	15	1.0%	3.0%	4.0%
5.25	0	10.0%	13.0%	4.0%
5.25	4	8.0%	12.0%	5.0%
5.25	6	6.0%	12.0%	5.0%
5.25	8	4.0%	9.0%	6.0%
5.25	12	1.0%	9.0%	6.0%
5.25	15	0.8%	6.0%	7.0%
7.875	0	0.6%	3.4%	14.0%
7.875	4	0.0%	2.0%	12.0%
7.875	6	0.0%	1.0%	9.0%
7.875	8	0.0%	0.5%	6.0%
7.875	12	0.0%	0.1%	4.0%
7.875	15	0.0%	0.1%	3.0%

The next step is to make a Weibull distribution fit on the data. To do so first is calculated a long-term distribution of pressure and after, fitted a linear tendency line. The *a* and *b* parameters of this line are then converted in *h* and *q* for the distribution. Finally, the Weibull Distribution or the cumulative frequency of each pressure for each sailing case is plotted (Figure 7.5).

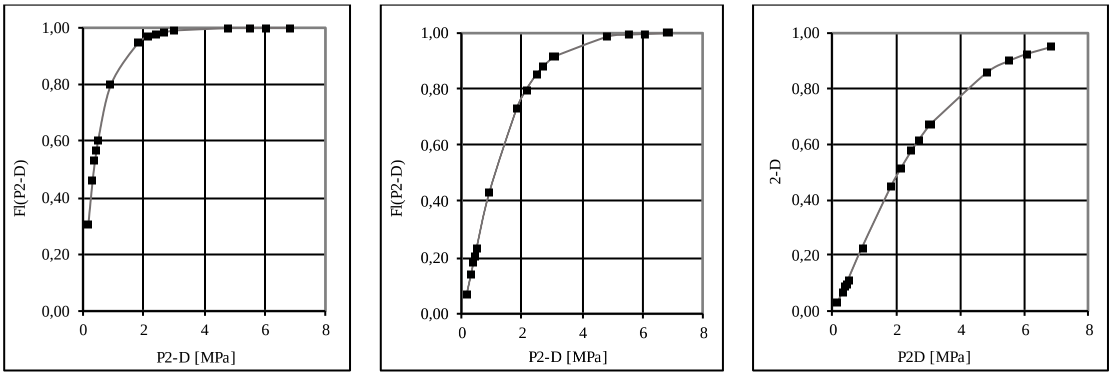

(a) Basic User (b) Intermediate User (c) Master User

Figure 7.5: Weibull Distribution for the three user profiles

As expected, the basic user shows a higher probability of generating smaller pressures on the fin. For the remaining users, the slope shifts to more considerable pressures, indicative of how each profile manages its velocity/angle and associated pressure interval. These graphs are indicative and shall be used on a later analysis, which will combine fatigue results.

7.3 Notes on Water Tunnel Results

Parallel to the CFD investigation, at the Emerson Cavitation Tunnel, in Newcastle University, water tunnel tests have been conducted by Katherine Tansley [29].

On her research was used the same fin like the one used on this work. The flow speed and angle of attack are changed to perform several hydrodynamic conditions. The analysis focused on the flow around the fin and the flow transition on the surface. The loads are obtained with a six-component load cell. The integral description of the assembly may be found at the disclosed work. The main conclusions state that the fin enters in stall at 8° of AoA and lift is the main force contributing to the resultant of forces. Additionally, it is verified that the fin tip deflects and that this deflection rises with the flow velocity and AoA. This is an important conclusion, as the fin geometry changes, so do the behaviour of the flow. It means that the results taken by CFD analysis will lack this phenomenon, and those results will not portrait a realistic scenario. It will be vital to perform a Fluid-Structure Interaction analysis to be closer to the real-life model.

It is also interesting to verify that the deflection does not seem to decrease after the fin stalls, as one would expect after a reduction in lift.

The lift measurements are also hard to predict after 7°/8° AoA and lift is seen to be decreasing after 13.5°. The results of the lift coefficient/lift force will be posteriorly compared when more data from the CFD analysis is concluded, although the reader must bear in mind the differences in experimental and analytical results.

Chapter 8

Conclusion

The objective of this thesis was to perform a hydrodynamic analysis and find how much load was at play on a slalom fin of windsurf board. Since the shape of the fin's hydrofoil cannot be fit into any standard, like NACA for instance, it was mandatory to have a method to validate and calibrate the three-dynamic analysis, instead of tackling the problem directly. Thus, the task was divided into smaller tasks.

The first task was intended to feel in which regime the flow fitted. This is important, as later on explained, to select the most appropriate physical model. In this first task, the program XFOIL was used. The reasons to use XFOIL are multiple: it was chosen for being an open use software, and also because most of the remaining programs use the same code foundation. It is also simple and easy to use. Firstly, using a known aerofoil as control (an Eppler 387), the outputs from the program were compared to real wind tunnel experiments. The choice of control aerofoil was set not because of its geometry but because of the data available, which was inside the same Reynolds number interval. Knowing the abilities and limitations of the program from the simulation, the results from the fin hydrofoil were extracted. This was, most times, a hard task because the convergence of results proved difficult for AoA's between 4° and 5°. It was also needed to input a modification on the geometry of the foil, to fix a Computer Aided Design problem. This small difference in the profile geometry also shows how the manufacturing process is determinant. Unfortunately, XFOIL cannot characterise laminar separation bubbles, and that was understood as the reason for the difficulty felt to converge certain angles.

From those notes, the second part of the three-part objective was outlined. It was clear that a transition model would have to be used, due to the flow regime and to the hint from the non-convergence of results. A 2-D study was developed to understand which model would provide the most accurate solution. To accomplish the job, the CFD program Star-CCM+ was used; a very intuitive software available for researchers at the LASEF laboratory, in Lisbon. Again, the control aerofoil was used for validation and determined that using RANS, the SST $k - \omega$ Turbulence Model and the add-on $\gamma - Re\theta$ Transition Model would be a possible way to start the analysis. Of course, there are many different models and solvers, each best suited for specific purposes. There are many more combinations, although verifying each would take an extended period.

Attention was given to the mesh characterisation. The domain was divided into volumes, all delimitating the space surrounding the foil. This way, the dimension of the mesh around the foil could be fine-tuned, to meet the needs of the physics model and present quality results. The most vital of these needs is to have a good boundary layer definition to capture the transition effects. Thus, the mesh immediately around the foil needs to be constant and very fine. The method to access this is by having a Wall Y^+ parameter not more than 1.

In the end, lift and pressure distributions are accurate with the chosen physics' models but should be kept in consideration that drag is represented with an error of 5%. The results with the SFWB hydrofoil revealed there was, in fact, a recirculation bubble that the XFOIL failed to represent.

There were some issues regarding 2-D solutions. From previous literature and knowledge, it was expected that the foil would shed vortexes. After intensive research, the only vortexes generated where at the first stages of the simulation, before the solution was converged. After several seconds into the simulation, there were still no signs of vortex street. This conclusion was also supported by the absence of significant pressure or force variations. It is believed that the flow does have instability, especially for larger AoA's, but one or both of the next possibilities might be occurring: either the mesh is too coarse to capture instability phenomenon like a Kelvin Helmholtz, or an unknown error was occurring during the simulation. Regardless, the results from validation propose that the simulation was well carried out.

Using the Star CCM+ results from the 2-D analysis from the fin, a mesh convergence study was done. It was possible to reduce the number of cells in about 75% and keep the results inside an error margin of 5%. The most sensible parameter being the drag.

Having gathered another critical parameter, the 3-D simulation was assembled. It was designed with all the notes and results from the previous chapters. Although the first goal was to use the mesh parameters as closer to the previous simulations, it proved hard to include the third control volume, that added a very fine mesh to the leading and trailing edge of the fin. This mesh was made to compensate for the acute edges of the foil, that, due to its radius, deformed the important cells at these areas. It was, eventually, obtained a simulation with around 10M cells.

Simulations at 3-D stage progress at a smaller pace than 2-D simulations, and, because of this and other factors, only one simulation case is included on this thesis. The results from the first condition are unveiling results close to the two-dimensional analysis, and displaying the same flow characteristics, like the LSB.

In what concerns the parametric optimisation studies, no advantages are seen when changing the maximum thickness or its position. The path was also opened for later study of user profiles, that will need to be coordinated with a FEM analysis to the fin itself. The latter is presently being developed.

Finally, the parallel research in Newcastle at the cavitation tunnel shows that the fin stalls at about 8° of AoA, a number met by this thesis simulations. It also shows that the most critical force in the force resultant, measured in the SFWB, is the lift. The drag force only becomes more expressive after reaching 14°, where it increases rapidly. The fin also deflects with the hydrodynamic forces. Even after the fin stalls, the deflection does not seem to reduce, as would be expected from the lack of lift force.

Chapter 9

Future Work

Concerning the next steps of the present work, there are some main points of focus that would be interesting to explore.

This thesis may be extended in what concerns the 3-D simulation. More cases are under development and when done, should provide an insight of the fin behaviour. The results will then be compared to the real-life results obtained at the cavitation tunnel.

The remaining works being developed by peers are a good add-up for the understanding of the fin. The finite element analysis that follows the hydrodynamic study in this work is already using the data provided. In the future, it is also possible to pursue a fluid-structure interaction study, as first intended, and vital to correctly model what occurs to the fin. This will provide results, not only for hydrodynamic and structural behaviour but also, in real time, apply torsion. Due to this, it will be possible to see the forces in the fin and how it flexes and bends back and changes the fluid. With this dynamic, it will come clearer why and how the fin is breaking and make a more accessible path to work on optimisation.

The hydrodynamic analysis also provided the tools and instructions for fin makers to reproduce the water effects in a non-destructive test. With this, it will be possible to achieve an enhanced fin, saving money in tests. This optimisation will give the real users improved speed and balance, as well as an overall better-quality product for less price.

Regarding competition, it will prove to be the future tool for improving this vital part of the windsurf board. Fins will be tailored for the players in less time, helping teams reach higher scores.

References

[1] T. Talay, "Introduction to the Aerodynamics of Flight," NASA, 1975. [Online]. Available: https://history.nasa.gov/SP-367/cover367.htm. [Accessed 30 May 2018].

[2] L. Sutherland, "Windsurf Fins," 2018. [Online]. Available: http://www.leighsutherland.com/index.html. [Accessed 2 May 2018].

[3] A. Center, "Technology, Invention and Innovation Collections," Archives Center, National Museum of American History, August 1999. [Online]. Available: https://web.archive.org/web/20150219204212/http://amhistory.si.edu/archives/d8625.htm. [Accessed 19 February 2015].

[4] Arne, "When to use the centreboard," 2013. [Online]. [Accessed 26 March 2018].

[5] I. Sailboards, "Windsurfing 101: Understand fundamentals of windsurfing boards & parts: Isthmus Sailboards," Isthmus Sailboards, 2018. [Online]. Available: https://isthmussailboards.com/windsurfing-101. [Accessed 26 March 2018].

[6] E. /. S. Team, "Windsurfing Fins Basics," EASY / SURF shop, [Online]. Available: https://easy-surfshop.com/do/page/buyingguide-fins. [Accessed 27 March 2018].

[7] F. Moukalled, L. Mangani and M. Darwish, The Finite Volume Method in Computational Fluid Dynamics, vol. 113, Springer International, 2016.

[8] V. d. Brederode, Fundamentos de Aerodinâmica Incompressível, Lisboa: Author's edition, 1997.

[9] N. M. Silva, Parametric Design, Aerodynamic Analysis and Parametric Optimization of a Solar UAV, Lisbon: Instituto Superior Técnico, 2014.

[10] K. R. Atkins, Investigation into the flow behaviour of a NACA 0021 airfoil with leading edge undulations simulated with RANS in Star-CCM+, Manchester: School of Mechanical, Aerospace and Civil Engineering, 2015.

[11] F. Nascimento, Windsurf Fin- Numerical and Experimental Analysis of Ultimate Strength, Lisbon: Instituto Superior Técnico, 2017.

[12] M. H. Sharqawy, J. H. Lienhard and S. M. Zubair, "Thermophysical properties of seawater: A review and new correlations that include pressure dependance," *Desalination and Water Treatment,* vol. 16, pp. 354-380, April 2010.

[13] K. G. Nayar, M. H. Sharqawy, L. D. Banchik and J. H. Lienhard, "Thermophysical properties of seawater: A review and new correlations that include pressure dependance," *Desalination,* vol. 390, pp. 1-24, 2016.

[14] G. Cribb, "Tactics, Tuning and Technique," *Windsurf,* no. 298, 2010.

[15] N. Hall, "Navier-Stokes Equations," NASA, 5 May 2015. [Online]. Available: https://www.grc.nasa.gov/www/k-12/airplane/nseqs.html. [Accessed 2 April 2018].

[16] H. Strum, G. Dumstorff, P. Busche, Dieter Westermann and W. Lang, "Boundary Layer Separation and Reattachment Detection on Airfoils by Thermal Flow Sensors," *Sensors,* vol. 11, 2012.

[17] H. Y. Mark Drela, *Xfoil 6.94 User Guide,* 2001.

[18] M. Hepperle, "Martin Hepperle," Dr. Martin Hepperle, 27 January 2007. [Online]. Available: https://www.mh-aerotools.de/airfoils/javafoil.htm. [Accessed 1 March 2017].

[19] Varius, "XFLR5," 7 January 2018. [Online]. Available: http://www.xflr5.com/xflr5.htm. [Accessed 1 March 2018].

[20] S. B. W. a. F. B. M. J. R. MCGhee, Experimental Results for the Eppler 387 Airfoil at Low Reynolds Numbers in the Lagley Low-Turbulence Pressure Tunnel, NASA TM-4062, 1988.

[21] I. ANSYS, "ANSYS Fluent Sonftware: CFD Simulation," ANSYS, Inc, 2018. [Online]. Available: https://www.ansys.com/products/fluids/ansys-fluent. [Accessed 17 August 2018].

[22] Siemens, "STAR-CCM+ |MDX," Siemens, 2018. [Online]. Available: https://mdx.plm.automation.siemens.com/star-ccm-plus. [Accessed 17 August 2018].

[23] O. L. (. Group), "OpenFOAM(R) - Official home of The Open Source Computational Fluid Dynamics (CFD) Toolbox," OpenCFD Ltd, 2018. [Online]. Available: https://www.openfoam.com/. [Accessed 16 August 2018].

[24] S. M. A. Aftab, A. S. Mohd Rafie, N. A. Razak and K. A. Ahmad, "Turbulence Model Selection for Low Reynolds Number Flows," *PLos ONE,* vol. V. 11 (4), 2016.

[25] F. R. Menter, "Two-equation eddy-viscosity turbulence models for engineering applications," vol. 32, no. 8, pp. 1598-1605, 1994.

[26] R. B. a. M. F. R. Langtry, "Correlation-based transition modeling for unstructured parallelized computational fluid dynamics codes," *AIAA,* vol. 47, no. 12, pp. 2894-2906.

[27] F. R. Menter, R. Langtry, S. Likki, Y. Suzen, P. Huang and S. Volker, "A correlation-based transition model using local variables—Part I: model formulation," *Journal of turbomachinery,* vol. 128, no. 3, pp. 413-422, 2006.

[28] P. Lissaman, "Low-Reynolds-number airfoils," *Annual Review of Fluids Mechanics,* vol. Vol. 15, no. no. 1, pp. pp. 223-239, 1983.

[29] K. Tansley, "Investigation into Windsurf Fin Hydrodynamics - A practical Study," Newcastle University, Newcastle, 2018.

Appendix A

A.1 P113 Coordinates

x	y	x	y	x	y	x	y	x	y
1	0.00065	0.58803	0.03723	0.16348	0.03195	0.17665	-0.03309	0.60132	-0.03664
0.99453	0.00138	0.57475	0.03778	0.15032	0.03071	0.18985	-0.03414	0.6146	-0.03601
0.98425	0.00275	0.56146	0.03829	0.13717	0.02937	0.20305	-0.0351	0.62788	-0.03535
0.9716	0.00446	0.54818	0.03877	0.12405	0.02791	0.21627	-0.03597	0.64116	-0.03464
0.95867	0.0062	0.53489	0.0392	0.11096	0.02633	0.2295	-0.03677	0.65443	-0.03389
0.94561	0.00793	0.5216	0.03959	0.09788	0.02462	0.24273	-0.03749	0.6677	-0.03311
0.93251	0.0096	0.50831	0.03993	0.08489	0.02277	0.25597	-0.03813	0.68098	-0.03229
0.91934	0.01119	0.49502	0.04024	0.07195	0.02075	0.26922	-0.03871	0.69425	-0.03142
0.90618	0.0127	0.48173	0.04051	0.0589	0.0185	0.28248	-0.03922	0.70751	-0.03053
0.89299	0.01413	0.46844	0.04074	0.04627	0.01608	0.29574	-0.03967	0.72078	-0.02959
0.87977	0.01552	0.45514	0.04092	0.03422	0.01349	0.309	-0.04005	0.73404	-0.02861
0.86653	0.01688	0.44185	0.04107	0.02222	0.0105	0.32227	-0.04038	0.7473	-0.0276
0.85329	0.0182	0.42856	0.04117	0.011	0.00713	0.33555	-0.04065	0.76056	-0.02656
0.84004	0.0195	0.41527	0.04123	0.00428	0.00444	0.34883	-0.04086	0.77382	-0.02547
0.8268	0.02077	0.40198	0.04125	0.00116	0.0023	0.36211	-0.04103	0.78707	-0.02436
0.81355	0.022	0.38869	0.04122	0.00012	0.00069	0.3754	-0.04115	0.80031	-0.0232
0.80031	0.0232	0.3754	0.04115	0.00012	-0.00069	0.38869	-0.04122	0.81355	-0.022
0.78707	0.02436	0.36211	0.04103	0.00116	-0.0023	0.40198	-0.04125	0.8268	-0.02077
0.77382	0.02547	0.34883	0.04086	0.00428	-0.00444	0.41527	-0.04123	0.84004	-0.0195
0.76056	0.02656	0.33555	0.04065	0.011	-0.00713	0.42856	-0.04117	0.85329	-0.0182
0.7473	0.0276	0.32227	0.04038	0.02222	-0.0105	0.44185	-0.04107	0.86653	-0.01688
0.73404	0.02861	0.309	0.04005	0.03422	-0.01349	0.45514	-0.04092	0.87977	-0.01552
0.72078	0.02959	0.29574	0.03967	0.04626	-0.01608	0.46844	-0.04074	0.89299	-0.01413
0.70751	0.03053	0.28248	0.03922	0.0589	-0.0185	0.48173	-0.04051	0.90618	-0.0127
0.69424	0.03142	0.26922	0.03871	0.07195	-0.02075	0.49502	-0.04024	0.91934	-0.01119
0.68098	0.03229	0.25597	0.03813	0.08489	-0.02277	0.50831	-0.03993	0.93251	-0.0096
0.6677	0.03311	0.24273	0.03749	0.09788	-0.02462	0.5216	-0.03959	0.94561	-0.00793
0.65443	0.03389	0.2295	0.03677	0.11096	-0.02633	0.53489	-0.0392	0.95867	-0.0062
0.64115	0.03464	0.21627	0.03597	0.12405	-0.02791	0.54818	-0.03877	0.9716	-0.00446
0.62788	0.03535	0.20305	0.0351	0.13717	-0.02937	0.56146	-0.03829	0.98425	-0.00275
0.6146	0.03601	0.18985	0.03414	0.15032	-0.03071	0.57475	-0.03778	0.99453	-0.00138
0.60132	0.03664	0.17665	0.03309	0.16348	-0.03195	0.58803	-0.03723	1	-0.00065